https://doi.org/10.5194/ar-2026-52
Preprint. Discussion started: 24 November 2026
© Author(s) 2026. CC BY 4.0 License.



AEROSOL Research Discussions

An automated computer vision framework for the systematic sizing and kinematic analysis of multiple droplets in ultra-high-speed videos

Carlos Pérez-Cantalapiedra[1,2], Manuel Carranza-García[1], Luis B. Modesto-López[2,*]

[1]*Department of Computer Languages and Systems, ETSII, University of Sevilla, Av. de la Reina Mercedes s/n, 41012 Seville, Spain*
[2]*Department of Aerospace Engineering and Fluid Mechanics, ETSI, University of Sevilla, Camino de los Descubrimientos s/n, 41092 Seville, Spain*

Correspondence to: Luis B. Modesto-López (lmodesto@us.es)

ORCID: C. Pérez-Cantalapiedra 0009-0002-6219-1044; M. Carranza-García 0000-0002-4729-8604; L. B. Modesto-López 0000-0002-9493-8846.

Abstract. Measuring the size and motion of individual droplets in sprays remains challenging when many droplets coexist, overlap, or cross paths in ultra-high-speed recordings. We present Droplet Analyzer (DA), an automated open-source framework built on OpenCV that combines droplet detection, geometric characterization, trajectory reconstruction, and two-dimensional velocity estimation, and preserves the link between size, position, and velocity for each droplet. Performance was quantified with synthetic sequences with prescribed droplet sizes, positions, and velocities, processed with a configuration selected on an independent tuning set. Droplets of 4 pixels (px) and larger were detected under moderate noise, relative sizing errors were below 10% for diameters of at least 15 px, and velocity errors for isolated droplets remained below 2.4% for displacements of about 1.5 px per frame or more. Increasing scene density mainly degraded trajectory continuity. For a published Flow Blurring condition, DA median diameters (36.6–40.7 µm) were within 1–2 px of those obtained with an earlier image-analysis method and of the same order as laser-diffraction measurements. DA was then applied to electrically assisted Flow Blurring sprays from injectors with 700 and 900 µm orifices at seven voltages between 0 and 12 kV, using 3208 trajectories from 50 recordings. At 12 kV, the volume median diameter decreased by 62% and 36% for the 700 and 900 µm injectors, respectively, and local volume median diameters decreased in all sampled transverse regions, whereas the number median remained nearly constant and the 90th percentile of the diameter decreased. Droplet velocity decreased with increasing diameter and showed no systematic dependence on voltage. Trajectory-resolved imaging thus separates changes in the larger droplets from those in the bulk population and resolves how the size distribution varies across the spray. These droplet-level data are relevant to aerosol generation and to the subsequent transport and deposition of the droplets.

1. Introduction

The size, velocity, and trajectory of droplets are key parameters that characterize the kinematics of liquid atomization-based multiphase flows, and they are relevant to technologies such as spray combustion, agricultural spraying, coating, inkjet printing, and microfluidic processes (Lefebvre and McDonell, 2017). For instance, in spray combustion, inadequate atomization produces relatively large droplets, resulting in lower evaporation rates and deficient fuel-air mixing, with direct implications for ignition behavior, heat release, and pollutant formation (Sirignano, 2010). In agricultural spraying, droplet size and velocity determine application quality and off-target losses (Nuyttens, 2007; De Cock et al., 2016). In some applications, electrical forces are also used to control sprays, since electrostatic charging can enhance droplet deposition on

https://doi.org/10.5194/ar-2026-52
Preprint. Discussion started: 24 November 2026
© Author(s) 2026. CC BY 4.0 License.



target surfaces (Law, 2001). Moreover, in electrohydrodynamic atomization (Gañán-Calvo et al., 2018), electrical stresses drive liquid deformation, jet formation, and breakup, principles exploited in electrospray ionization mass spectrometry (Fenn et al., 1989), thin-film deposition, encapsulation, and the production of micro- and nanoparticles (Jaworek, 2007; Jaworek and Sobczyk, 2008). In such applications the droplet population leaving the atomizer is the source of an aerosol, and its size distribution influences the evaporation rate of the droplets, their transport and deposition, and, in cases where the liquid carries solutes or particles, the size of the residual particles. The experimental characterization of these sprays therefore requires diagnostic techniques that provide quantitative and spatially resolved information on droplet populations, which is also needed to validate predictive numerical models.

Conventional characterization of droplet size distributions (DSD) has largely relied on phase-Doppler techniques and laser diffraction. Phase-Doppler particle analysis (PDPA) provides accurate local measurements of droplet size and velocity, but these are restricted to a small sample volume and do not give direct access to the instantaneous spatial organization of the spray (Privitera et al., 2023; Sijs et al., 2021). Laser diffraction provides robust ensemble DSDs but does not resolve individual droplets or their trajectories. Neither technique captures droplet morphology or the transient evolution of ligaments and breakup structures.

Image-based approaches, particularly high-speed shadowgraphy and backlit imaging, visualize many droplets simultaneously within a two-dimensional (2D) field of view and, combined with suitable tracking algorithms, provide the size, position, trajectory, and velocity of individual droplets. Castanet et al. (2013) showed that high-speed shadow imaging can measure droplet size and velocity simultaneously, while highlighting the practical difficulties associated with blurred contours, droplet deformation, overlap, and depth-of-field effects. De Cock et al. (2016) developed a shadow-imaging method for agricultural sprays that includes background correction and a focus criterion based on edge gradients to reject out-of-focus droplets, and Basu (2013) showed that the fidelity of the measured droplet shape improves as the number of pixels resolving each droplet increases. These difficulties become more severe as the droplet concentration increases. In the near field of dense sprays, optical density limits what visible-light imaging can resolve (Bothell et al., 2020; Li et al., 2019), and X-ray techniques penetrate the spray at the cost of more complex instrumentation, limited accessibility, or a reduced field of view (Bothell et al., 2020). Visible-light imaging is therefore most reliable where droplets are sufficiently separated, in focus, and well contrasted to be resolved individually in the image plane.

Even under these favorable conditions, the processing of large high-speed (HS) video datasets remains a major challenge. Modern HS cameras generate thousands of frames containing many droplets, which makes manual or semi-manual processing impractical and potentially biased, and classical pipelines based on thresholding, edge detection, morphological operations, or watershed-type separation often require case-specific tuning and are sensitive to non-uniform illumination, image noise, and scene density (Castanet et al., 2013; De Cock et al., 2016). Recent efforts have therefore shifted toward automated image-analysis frameworks that reduce user intervention and improve reproducibility across experimental conditions. Open-source tools are particularly valuable in this respect, because they lower implementation costs and ease the transfer of methods between laboratories, and OpenCV (Open Source Computer Vision Library) combines image filtering, segmentation, contour detection, morphological processing, and object tracking in a single widely used library (Bradski, 2000).

A demanding application for such tools is the characterization of sprays generated by twin-fluid atomizers, of which Flow Blurring (FB) is a particularly efficient example. In FB atomization, part of the atomizing gas flows back into the liquid-feeding tube and generates a turbulent two-phase mixture upstream of the discharge orifice, from which a fine spray emerges (Gañán-Calvo, 2005; Rosell-Llompart and Gañán-Calvo, 2008). The technique has been used, for example, for the clean

https://doi.org/10.5194/ar-2026-52
Preprint. Discussion started: 24 November 2026
© Author(s) 2026. CC BY 4.0 License.



combustion of viscous liquid biofuels (Simmons and Agrawal, 2012). Atomization can also be assisted electrically, as in charge-injection atomizers, developed mainly for electrically insulating liquids such as hydrocarbon fuels. In these devices, an electrode immersed in the liquid upstream of the orifice introduces electrical charge, allowing electric forces to influence liquid breakup and the subsequent dispersion of droplets, thus providing an additional means of tailoring droplet populations alongside the action of the atomizing gas (Shrimpton and Yule, 2003; Shrimpton, 2009). Combining an immersed electrode with FB atomization introduces this electrical contribution into a primarily pneumatic process. Its effect may depend on droplet size and position in the spray, so it is not necessarily captured by a single size distribution. Characterizing this response requires measurements near the point of generation that retain the size, position, and velocity of individual droplets, which makes electrically assisted FB sprays a suitable application for trajectory-resolved image analysis.

The present work addresses these challenges by introducing Droplet Analyzer (DA), an automated computational framework based on OpenCV for the systematic analysis of multiple droplets in ultra-high-speed (UHS) videos. The proposed methodology combines deterministic image-processing operations with spatiotemporal tracking in a unified workflow, enabling droplet detection, geometric characterization, trajectory reconstruction, and 2D velocity estimation while preserving the association between droplet size, morphology, position, and velocity.

The framework is evaluated using synthetic sequences with known droplet properties and compared with previously published FB measurements. It is then applied to electrically assisted FB sprays recorded at ultra-high frame rates to examine how droplet size and velocity vary with applied voltage and transverse position. By combining number-based and volume-based statistics with individual droplet trajectories, the study demonstrates the capabilities of DA for spatially resolved characterization of aerosol sources and provides experimental insights into the response of a primarily pneumatic atomization process to electrical assistance.

2. Materials and Methods

2.1. A computational framework for droplet detection, sizing, and tracking

Droplet Analyzer (DA) was developed to process UHS videos acquired during, but not limited to, liquid atomization experiments. Although the present study focuses on droplets generated by a Flow Blurring (FB) atomizer, the proposed workflow can be readily adapted to other HS imaging applications involving dispersed droplets. The framework was designed to extract geometric descriptors of individual droplets from individual frames and subsequently reconstruct droplet trajectories and estimate kinematic parameters across image sequences. The workflow comprises image preprocessing, droplet segmentation, contour-based filtering, feature extraction, tracking, velocity estimation, and data export.

OpenCV (Bradski, 2000) provides optimized implementations of the main image-processing operations required by the workflow, including grayscale conversion, contrast enhancement, denoising, adaptive thresholding, morphological filtering, contour extraction, and geometric measurements. Its open-source architecture also facilitates reproducible implementation and adaptation of the processing pipeline to different imaging conditions.

The complete workflow was implemented in a modular class, which receives a UHS video as input, processes the frames sequentially, and stores the extracted information in a structured format for subsequent analysis. As illustrated in Fig. 1, the framework is organized into three main phases: 1) preprocessing; 2) segmentation, filtering, and geometric characterization; and 3) tracking, velocity estimation, and data export. The modular architecture allows individual procedures to be modified or replaced without altering the overall workflow, thereby facilitating its adaptation to recordings acquired under different optical and experimental conditions. In the final phase, droplet velocities are first estimated from frame-to-frame centroid

https://doi.org/10.5194/ar-2026-52
Preprint. Discussion started: 24 November 2026
© Author(s) 2026. CC BY 4.0 License.

displacements in image coordinates and subsequently converted to physical units using the spatial calibration and the known inter-frame time.

Three structured data containers were defined to store the user-configurable processing parameters, intermediate results for each processed frame, and final results obtained after trajectory reconstruction. The implementation includes dedicated methods for preprocessing, segmentation, tracking, velocity estimation, result export, and diagnostic image generation. For each tracked droplet, the retained variables include frame index, centroid coordinates, projected area, equivalent diameter, circularity, roundness, and velocity components, among other descriptors. All user-configurable parameters, the values used in this work, and the settings that are fixed in the implementation are listed in Supplementary Table S1.

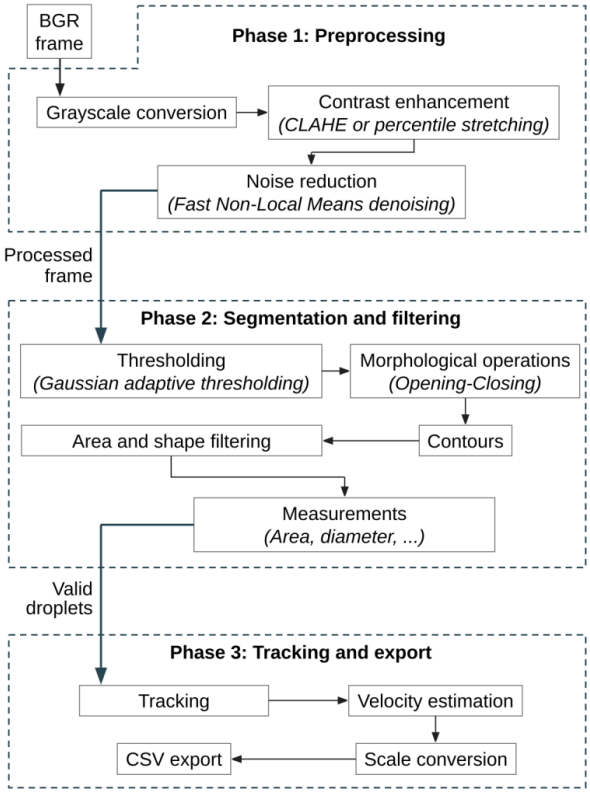

Figure 1. High-level workflow of Droplet Analyzer for automated droplet detection, sizing, tracking, and data export. The processing pipeline comprises image preprocessing, segmentation and contour-based filtering, geometric characterization, trajectory reconstruction, velocity estimation, and data export.

2.1.1. Image preprocessing

Image preprocessing constitutes the first stage of the computational workflow and aims to improve image quality prior to droplet segmentation by enhancing contrast and reducing noise, thereby facilitating the identification of droplet boundaries in subsequent steps. In the implemented workflow, preprocessing consists of three main operations: grayscale conversion, contrast enhancement, and noise reduction.

Grayscale conversion

https://doi.org/10.5194/ar-2026-52
Preprint. Discussion started: 24 November 2026
© Author(s) 2026. CC BY 4.0 License.



AEROSOL Research Discussions

Although the input videos are decoded by OpenCV as three-channel BGR frames, the acquired images are effectively monochromatic. Therefore, each frame is converted to a single grayscale channel to reduce computational cost and simplify subsequent processing. This transformation is also consistent with the following stages of the workflow, since thresholding, morphological operations, and contour extraction are performed on single-channel images. The conversion is performed using the OpenCV function cv2.cvtColor (Bradski, 2000).

Contrast enhancement

A significant fraction of the recorded frames exhibits limited contrast, which can hinder reliable identification of droplet boundaries. To address this issue, two histogram-based contrast-enhancement techniques were implemented: Contrast Limited Adaptive Histogram Equalization (CLAHE) (Zuiderveld, 1994) and percentile-based histogram stretching. CLAHE operates locally and allows the contrast limit to be adjusted, whereas histogram stretching was implemented by clipping the darkest 0.4% and brightest 0.4% of pixels and subsequently rescaling the intensity range between the corresponding percentiles. The user can select either method and adjust the associated parameters through the graphical interface. The CLAHE tile grid is fixed at 8 × 8 tiles. If both percentiles coincide, as occurs when the droplets occupy less than 0.4% of an otherwise uniform frame, the frame is left unstretched to avoid a degenerate rescaling.

Histogram stretching generally produces stronger global contrast enhancement and may improve droplet–background separation in low-contrast videos. However, it may also amplify image noise and local illumination artifacts. By contrast, CLAHE provides a more localized and controlled correction and may therefore be preferable when contrast degradation is moderate or excessive noise amplification must be avoided.

Noise reduction

After contrast enhancement, high-frequency noise and isolated pixel artifacts may become more pronounced, particularly when histogram stretching is applied. To reduce these effects, a Fast Non-Local Means denoising algorithm (Buades et al., 2011) was implemented using the OpenCV function cv2.fastNlMeansDenoising. This method attenuates noise while preserving image structures more effectively than simple local averaging filters. The denoising strength is user-configurable, allowing the degree of smoothing to be adapted to the characteristics of each video. Non-Local Means estimate each pixel from a weighted combination of similar image patches, thereby reducing random noise while preserving edges. The template and search windows are kept at the OpenCV defaults (7 and 21 px), so that only the filter strength h is exposed to the user.

The denoising stage reduces much of the noise introduced or amplified during contrast enhancement. However, excessive denoising may smooth the contours of the smallest or most poorly focused droplets. The denoising parameter must therefore be selected as a compromise between background-noise suppression and preservation of droplet-edge definition. Representative examples of the effect of each preprocessing step on the same source frame are shown in Fig. 2.

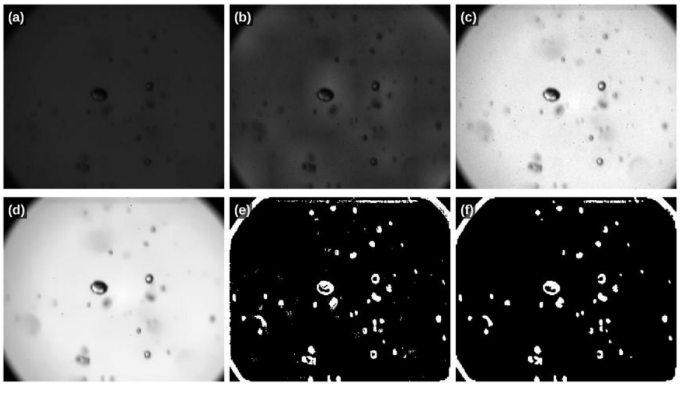

https://doi.org/10.5194/ar-2026-52
Preprint. Discussion started: 24 November 2026
© Author(s) 2026. CC BY 4.0 License.



AEROSOL Research Discussions

Figure 2. Representative effects of the preprocessing and segmentation operations applied to the same UHS frame. (a) Original grayscale image, (b) contrast enhancement using CLAHE, (c) percentile-based histogram stretching, (d) Fast Non-Local Means denoising, (e) binary mask obtained by Gaussian adaptive thresholding, and (f) final binary mask after morphological opening and closing.

2.1.2. Segmentation and contour-based filtering

The segmentation and filtering stage constitutes the core of the framework, as it determines which image regions are ultimately classified as droplets and passed to the measurement and tracking stages (Fig. 3a). This stage comprises adaptive thresholding, morphological processing, contour extraction, and geometric filtering.

Adaptive thresholding

Once a frame has been preprocessed, droplets must be separated from the background. For this purpose, Gaussian adaptive thresholding was implemented using the OpenCV function cv2.adaptiveThreshold. In the resulting binary image, droplet pixels are assigned to the foreground and the remaining pixels to the background. A local adaptive method was selected because it is less sensitive to spatial variations in illumination than a single global threshold. The block size and subtraction constant C are specified by the user.

The binary frames generated at this stage are not expected to provide perfect segmentation, particularly for small, blurred, or out-of-focus droplets. Rather, thresholding provides an initial estimate of the droplet regions, which is subsequently refined through morphological operations and contour-based filtering.

Morphological operations

To remove isolated binary noise and close small gaps within segmented droplets, two morphological operations are applied sequentially: opening followed by closing. Both operations are implemented using the OpenCV function cv2.morphologyEx with an elliptical structuring element whose size can be adjusted by the user. Opening primarily removes isolated foreground artifacts, whereas closing fills small residual gaps within segmented droplets and improves region continuity.

This sequence improves the binary mask prior to contour extraction. Opening may slightly erode droplet boundaries, particularly for small objects, whereas subsequent closing can restore local boundary continuity and reduce fragmentation. The kernel size must therefore be selected carefully to avoid removing small droplets or artificially merging neighboring objects.

Contour extraction

After morphological processing, droplet contours are extracted in two passes using the OpenCV function cv2.findContours, based on the Suzuki–Abe border-following algorithm (Suzuki and Abe, 1985). In the first pass, external contours are identified and filled to generate a binary mask without internal holes. Contours are then re-extracted from this filled mask in a second pass, yielding the final contour representation used for geometric characterization. The first pass uses a compressed representation of the contour points, whereas the second retains the complete contour description required for subsequent measurements.

This two-step procedure improves contour consistency and helps ensure that the measured objects correspond to filled droplet regions rather than hollow or fragmented structures. It also provides a consistent basis for subsequent measurements of projected area, equivalent diameter, perimeter-based circularity, and ellipse-based shape descriptors.

Area and shape-based filtering

Not all extracted contours correspond to physical droplets. Geometric filters are therefore applied to reject image artifacts, strongly deformed objects, and non-droplet structures before feature extraction. First, projected contour area is used to reject objects outside a user-defined minimum–maximum range. This criterion removes very small artifacts and isolated noise, as well as very large objects unlikely to correspond to individual droplets.

https://doi.org/10.5194/ar-2026-52
Preprint. Discussion started: 24 November 2026
© Author(s) 2026. CC BY 4.0 License.



Additional filtering is performed using circularity and roundness. Circularity is useful for identifying contours with irregular or fragmented boundaries, whereas roundness primarily characterizes the overall elongation of the detected object. These descriptors are complementary: a contour may exhibit reduced circularity because of pixelation, boundary roughness, or segmentation errors while retaining an approximately circular global shape, whereas elongated ligaments, merged droplets, or strongly deformed objects generally exhibit reduced roundness. The mathematical definitions of these descriptors are provided in the following section.

2.1.3. Droplet feature extraction

Once the final set of valid contours has been obtained, geometric descriptors are extracted for each detected droplet (Fig. 3b). The variables considered in the present implementation include centroid position, projected area, perimeter, equivalent diameter, circularity, roundness, bounding box, and binary mask. These descriptors are stored in a structured record for each processed frame, with one entry for each detected droplet, and are subsequently used for trajectory reconstruction, velocity estimation, diagnostic visualization, and data export.

The projected area and perimeter are obtained directly from the detected contour using the OpenCV functions cv2.contourArea and cv2.arcLength, respectively. The equivalent diameter, D_{eq}, is calculated as the diameter of a circle having the same projected area as the segmented droplet:

$$D_{eq} = 2 \cdot \sqrt{\frac{A}{\pi}} \quad (1)$$

where A is the projected contour area.

Circularity and roundness are used as complementary shape descriptors because they quantify different aspects of the segmented droplet shape (Russ, 2011). Circularity is computed as

$$C = \frac{4\pi A}{P^2} \quad (2)$$

where P is the contour perimeter. A value of unity corresponds to a perfectly circular contour. Because circularity depends directly on the measured perimeter, it is sensitive to local boundary irregularities, pixelation, blurred edges, and segmentation roughness.

Roundness is computed as

$$R = \frac{4A}{\pi MA^2} \quad (3)$$

where MA is the major axis of an ellipse fitted to the contour using cv2.fitEllipse. In contrast to circularity, roundness primarily characterizes the global elongation of the detected object. A value close to unity indicates a nearly circular projected shape, whereas lower values indicate increasing elongation or filament-like morphology. For contours containing fewer than five points, ellipse fitting cannot be performed and the roundness is set to zero.

The droplet centroid is obtained from image moments. For a binary region, the raw moment of order (p, q) is defined as

$$M_{pq} = \Sigma_x \Sigma_y x^p y^q I(x, y) \quad (4)$$

where $I(x, y) = 1$ for pixels inside the contour and $I(x, y) = 0$ elsewhere. The centroid coordinates are then calculated from the first-order moments as

$$c_x = \frac{M_{10}}{M_{00}}, c_y = \frac{M_{01}}{M_{00}} \quad (5)$$

where M_{00} is the zeroth-order moment, corresponding to the projected contour area in pixels (Hu, 1962; Russ, 2011). In practice, these quantities are calculated using the OpenCV function cv2.moments. If $M_{00} = 0$, the centroid is approximated by the center of the corresponding bounding box to avoid division by zero.

The bounding box is calculated from the contour coordinates using cv2.boundingRect. In addition, a binary mask is generated for each droplet by filling the corresponding contour on an otherwise empty image. This mask provides a local representation

https://doi.org/10.5194/ar-2026-52
Preprint. Discussion started: 24 November 2026
© Author(s) 2026. CC BY 4.0 License.



of the segmented object and can be used for diagnostic visualization, local intensity analysis, or subsequent validation. All extracted properties are stored in the record for each processed frame and propagated to the tracking and export stages.

2.1.4. Tracking, velocity estimation, and export

After segmentation and feature extraction, valid droplet detections are associated across frames to reconstruct individual trajectories. The tracking algorithm combines Lucas–Kanade optical-flow prediction with greedy nearest-neighbor association. For each active trajectory, the expected centroid position in the current frame is first predicted from the previous and current grayscale images using pyramidal Lucas–Kanade optical flow (Lucas and Kanade, 1981). Each detected droplet is then assigned to the closest unused trajectory whose reference position lies within the user-defined maximum tracking distance; when optical-flow prediction is unavailable, the last known centroid is used instead. A trajectory can remain available for reassociation for up to five frames, after which it is discarded if no compatible detection is found. Once a detection has been assigned, that trajectory is removed from the candidate set for the current frame, preventing multiple droplets from being linked to the same track. Unassigned detections initiate new trajectories. Lucas–Kanade prediction is applied to the unprocessed grayscale frames (15 × 15 px window, two pyramid levels, termination after 10 iterations or $\varepsilon = 0.03$) and is used only to guide the association; it is not used to compute velocities.

Each trajectory is represented by a track record containing the temporal evolution of the corresponding droplet across the image sequence. The stored variables include, among others, frame number, centroid position, equivalent diameter, circularity, roundness, and velocity components. This trajectory-based data structure provides the link between frame-wise image segmentation and time-resolved droplet analysis.

Droplet velocities are computed by finite differences of the centroid positions of consecutive detections within each track, $v_k = (x_{k+1} - x_k)/\Delta t_k$, where Δt_k is the number of elapsed frames divided by the acquisition rate; if a droplet is missed for up to five frames, the displacement is divided by the correspondingly longer interval. Each velocity is assigned to the first detection of the pair, so the last detection of a track carries no velocity. Velocities are obtained in px per frame and converted to physical units with the spatial calibration factor and the inter-frame time.

The resulting velocities should be interpreted as two-dimensional projected velocities within the imaging plane. Because the present configuration relies on single-camera backlit imaging, out-of-plane motion cannot be directly recovered and may result in changes in focus, contour sharpness, or track continuity. Consequently, short trajectories, abrupt variations in apparent diameter, or sudden changes in estimated velocity may indicate unreliable associations and should be considered during post-processing and validation.

The final output of the framework is exported in comma-separated-value (CSV) format for subsequent statistical analysis and visualization. The exported records allow the droplet population to be analyzed either frame by frame or trajectory by trajectory, enabling the construction of size and velocity distributions, size–velocity correlations, and spatially resolved velocity maps. An example of frame-to-frame association and the resulting reconstructed trajectories is shown in Fig. 3c.

DA retains the association between droplet size, projected-contour descriptors, position, and image-plane velocity along each reconstructed trajectory. Recording identifiers, trajectory identifiers, and frame information allow measurements to be traced to their source and summarized at trajectory, recording, and spatial-population levels.

https://doi.org/10.5194/ar-2026-52
Preprint. Discussion started: 24 November 2026
© Author(s) 2026. CC BY 4.0 License.

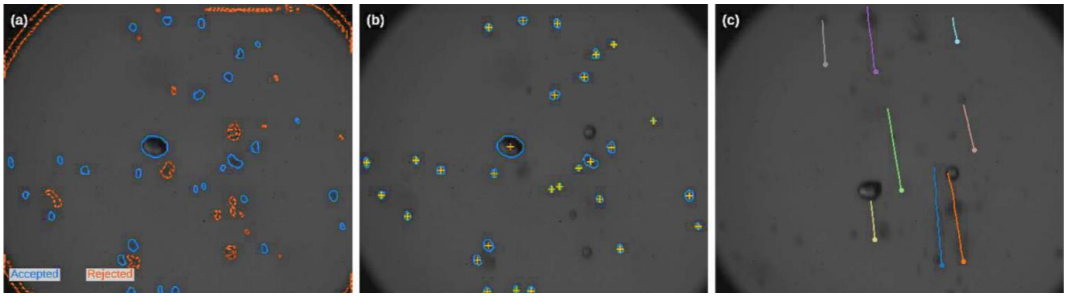

Figure 3. Example of droplet detection, filtering, and trajectory reconstruction. (a) Candidate contours after segmentation, distinguishing accepted droplets from rejected objects; (b) final droplet detections and centroid positions; and (c) reconstructed trajectories obtained by frame-to-frame association and used for velocity estimation.

2.2. Quantitative evaluation using synthetic video sequences

Quantitative assessment of measurement accuracy requires a ground truth (GT), which is unavailable in real atomization recordings because the actual droplet positions, diameters, and velocities are not independently known. To overcome this limitation, a dedicated synthetic-video generator was developed in Python. Each synthetic two-dimensional droplet was rendered as a dark disc on a bright background with a Gaussian-smoothed edge profile (σ_{edge} = 0.8 px), reproducing the dark droplet silhouettes of backlit imaging and, in a controlled manner, the finite edge sharpness encountered in high-speed imaging. Frames of 512 × 512 px were generated with background and droplet-core grey levels of 235 and 25, respectively. The center coordinates, velocity vector, and equivalent diameter of every droplet were prescribed exactly, so that the ground-truth data contain the frame-wise position, size, and velocity of each droplet. Additive Gaussian noise and salt-and-pepper corruption could be superimposed at configurable intensities to reproduce controlled levels of image degradation and to evaluate the robustness of the processing pipeline. Noise was added before clipping to the 8-bit range. Each video was generated with a fixed random seed and stored with a lossless codec (FFV1), so that the dataset can be regenerated bit for bit without compression artifacts. The generator, the ground-truth files, and the configuration of every sequence are provided with the source code.

Five experiments (E1–E5) were designed to assess distinct aspects of the framework. E1 assessed segmentation and sizing accuracy using static droplets with seven prescribed diameters, $d_{GT} = \{6, 10, 15, 20, 30, 40, 50\}$ px, in the absence of added noise. E2 evaluated velocity estimation using a single 20-px droplet moving at nine prescribed velocity vectors: five with whole-pixel displacements per frame in horizontal, vertical, and diagonal directions, two with sub-pixel components, (1.3, 0.7) and (4.25, −1.6) px/frame, and two slow motions of 0.4 and 0.2 px/frame, each without noise and with Gaussian noise of σ = 8. E3 assessed robustness to image degradation using a stationary 20-px droplet subjected independently to additive Gaussian noise with σ = {0, 5, 10, 20, 35, 50} and salt-and-pepper noise affecting 0, 2, 5, and 10% of the pixels. E4 assessed the detectable size range using single droplets with $d_{GT} = \{3, 4, 5, 6, 8, 10, 12, 15, 20, 25, 30, 40, 50, 60, 70, 80\}$ px under a fixed Gaussian-noise level of σ = 8. E5 evaluated scene-density effects using 60-frame sequences containing $N_d = \{5, 10, 20, 35, 50\}$ droplets of 18 px diameter moving simultaneously at 3 px/frame in randomly assigned directions under Gaussian noise with σ = 8. E1 sequences contained four droplets arranged on a 2 × 2 grid over 30 frames, whereas E2, E3, and E4 sequences contained a single droplet over 60, 40, and 30 frames, respectively. Velocities are expressed in px per frame. All five experiments were processed using a common parameter set (Table S1), selected beforehand using an independent tuning dataset. The configurations of the synthetic validation sequences and the tuning dataset are summarized in Table S2.

https://doi.org/10.5194/ar-2026-52
Preprint. Discussion started: 24 November 2026
© Author(s) 2026. CC BY 4.0 License.



AEROSOL Research Discussions

To avoid tuning the processing parameters on the sequences used for evaluation, a separate tuning set was generated with the same generator but different droplet diameters (5, 9, 14, 25, and 45 px), noise realizations (Gaussian noise with σ = 0, 10, and 25, and 5% salt-and-pepper noise), and droplet layouts (10 and 25 moving droplets of 16 px, and an isolated droplet moving at 6 px/frame). In a first stage, 96 combinations of contrast-enhancement method, Non-Local Means strength, adaptive-threshold block size and constant, and structuring-element size were evaluated. The three configurations with the highest mean F1-score were then combined with 12 combinations of minimum projected area and minimum circularity. Configurations were ranked by mean F1-score and, for practically equal F1-scores (difference below 0.005), by the mean $\mathrm{RMSE_d}$ defined below. Finally, the maximum association distance was selected on the moving-droplet sequences as the smallest value minimizing identity switches and track fragmentation (Fig. S1). The selected configuration (CLAHE with a clip limit of 2, h = 30, block size of 11 px, C = 5, 3 × 3 px elliptical structuring element, minimum area of 15 px^2, minimum circularity of 0.5, and maximum association distance of 15 px) reached a mean F1-score of 0.999 on the tuning set and was used without modification in E1–E5. E1–E5 characterize the pipeline against a known ground truth rather than reproduce a particular recording; the experimental videos of Sects. 3.2 and 3.3 were processed with parameter sets adapted to their imaging conditions (Supplementary Table S1), so that the trends identified here apply to them, whereas the absolute error values are indicative only.

For each sub-experiment, the complete analysis pipeline was executed programmatically through the Droplet Analyzer backend. Detected droplets were matched frame by frame to the corresponding ground-truth droplets using a greedy nearest-neighbor criterion without reassignment and with a maximum centroid distance of 15 px. A true positive (TP) corresponded to a detection successfully matched to a ground-truth droplet, a false positive (FP) to an unmatched detection, and a false negative (FN) to a ground-truth droplet for which no detection was found. Precision is the fraction of detections that are real droplets, P = TP/(TP + FP); recall is the fraction of real droplets that are detected, R = TP/(TP + FN). The F1-score is their harmonic mean, F1 = $2PR/(P + R)$, and equals 1 only if all droplets are detected with no false detections. TP, FP, and FN were accumulated over all frames of a sequence before computing P, R, and F1 (micro-averaging); averaging per-frame scores instead changed F1 by less than 0.02 in all sequences except the 3 px sequence of E4, in which each frame contributes a binary score. Sizing accuracy was quantified using the mean relative error and the root-mean-square error of the equivalent diameter:

$$\mathrm{MRE}_d = \frac{100}{N}\sum_{i=1}^{N}\frac{|d_i^{\mathrm{det}} - d_i^{\mathrm{GT}}|}{d_i^{\mathrm{GT}}},\ \mathrm{RMSE}_d = \left[\frac{1}{N}\sum_{i=1}^{N}\left(d_i^{\mathrm{det}} - d_i^{\mathrm{GT}}\right)^2\right]^{1/2}, \qquad (6)$$

where d_i^{det} and d_i^{GT} are the detected and ground-truth equivalent diameters of matched droplet i, respectively, and N is the number of matched detections. The mean signed bias, $b_\mathrm{d} = (1/N)\,\Sigma\,(d_\mathrm{i}^{\mathrm{det}} - d_\mathrm{i}^{\mathrm{GT}})$, was also computed to distinguish systematic over- or undersizing from random error, together with the mean circularity. For moving droplets, $\mathrm{MRE_v}$ and $\mathrm{RMSE_v}$ were computed analogously from the velocity magnitude of each matched detection and that of its ground-truth droplet, with $\mathrm{RMSE_v}$ expressed in px/frame. Tracking fidelity was quantified through the relative track-count deviation,

$$\Delta_{\mathrm{tracks}} = \frac{N_{\mathrm{tracks}}^{\mathrm{det}} - N_{\mathrm{tracks}}^{\mathrm{GT}}}{N_{\mathrm{tracks}}^{\mathrm{GT}}}, \qquad (7)$$

where N_{tracks}^{det} and N_{tracks}^{GT} are the numbers of reconstructed and ground-truth trajectories, respectively. The quantity is referred to here as the track-fragmentation index: a value of 0 corresponds to one-to-one reconstruction, positive values indicate trajectory fragmentation, and negative values indicate trajectory merging or loss. Because Δ_{tracks} compares only track counts, false-positive tracks, fragmented trajectories, and tracks that switch between droplets can partly compensate each other. Two association-based metrics were therefore added: the number of tracks per ground-truth droplet, defined as the mean number of distinct reconstructed tracks matched to each ground-truth droplet (1 for ideal tracking), and the number of identity switches, defined as the number of times the reconstructed track matched to a given ground-truth droplet changes between consecutive matched frames.

https://doi.org/10.5194/ar-2026-52
Preprint. Discussion started: 24 November 2026
© Author(s) 2026. CC BY 4.0 License.



AEROSOL Research Discussions

2.3. Experimental application to electrically assisted Flow Blurring

To demonstrate its applicability to experimental spray measurements, DA was applied to UHS recordings of electrically assisted FB atomization. Two injector geometries were investigated at several applied voltages to characterize droplet size, spatial distribution, and velocity.

2.3.1. Atomizer, working fluids, and operating conditions

In the conventional FB configuration (Gañán-Calvo, 2005; Rosell-Llompart and Gañán-Calvo, 2008), the liquid is supplied through a feeding tube whose exit is located a distance H upstream of a discharge orifice of diameter D, while the atomizing gas flows through the annular passage surrounding the tube and leaves through the orifice together with the liquid (Fig. 4a). The internal gas–liquid interaction that characterizes FB is strongly influenced by the geometric ratio H/D (Gañán-Calvo, 2005; Modesto-López and Gañán-Calvo, 2018). The two injectors used in this study, hereafter Injectors 1 and 2, were fabricated by additive manufacturing with nominal discharge-orifice diameters of 700 and 900 µm and a common nominal gap $H = 50$ µm, which gives $H/D = 0.0714$ and 0.0556, respectively.

Type II water was used as the working liquid and compressed air as the atomizing gas. The liquid volumetric flow rates were 4.062 and 19.722 mL/min for Injectors 1 and 2, with corresponding gas flow rates of 0.8047 and 2.33 L/min, which, for a reference gas density of 1.20 kg/m³, give gas-to-liquid mass ratios (GLR) of 0.2384 and 0.1422. The sprays were discharged vertically downward into ambient air at atmospheric pressure.

Each injector incorporated a stainless-steel needle electrode inside the liquid-feeding tube (Fig. 4a). The needle had a nominal length of 33 mm and a diameter of 0.9 mm, with a tapered section approximately 2.4 mm long, a nominal taper angle of 20.3°, and an estimated tip radius of curvature of 25 µm. A positive high voltage, V, was applied to the needle while a brass ring surrounding the atomizer outlet was grounded, which established an electric field between the two electrodes. The voltage was varied from 0 to 12 kV in steps of 2 kV, with $V = 0$ corresponding to conventional FB atomization and serving as the reference condition.

The water had an electrical conductivity, κ_l, of approximately 2.2 µS/cm, so its charge relaxation time is $\tau_e = \varepsilon_0 \varepsilon_r / \kappa_l \approx 3.2\,\mu s$, where ε_0 is the vacuum permittivity and $\varepsilon_r \approx 80$ is the relative permittivity of water. Electrical charge can therefore redistribute within the liquid by conduction on a microsecond timescale. The geometrical parameters, operating conditions, and fluid properties are summarized in Table 1.

2.3.2. Ultra-high-speed imaging and video acquisition

The sprays were recorded using a UHS imaging system previously employed by our group to study droplets, liquid ligaments, and polymeric filaments generated by FB and related atomization processes (Modesto-López and Gañán-Calvo, 2018; Modesto-López et al., 2019; Hermosín-Reyes et al., 2019; Ramos-Escobar et al., 2020; Marín-Brenes et al., 2021). The system comprised a Shimadzu HPV-2 camera fitted with an optical objective and a Walimex Pro Studio Flash (VC-4000) for illumination (Fig. 4b). The camera was positioned perpendicular to the spray axis, with the flash on the opposite side and synchronized with the camera by an external trigger. Recordings were acquired at 10^6 frames/s (1 µs between frames), with 102 frames per video.

The axial coordinate, x, was measured downstream from the discharge orifice along the main spray direction, whereas the transverse coordinate, r, was measured from the spray centerline within the imaging plane (Modesto-López and Gañán-Calvo,

https://doi.org/10.5194/ar-2026-52
Preprint. Discussion started: 24 November 2026
© Author(s) 2026. CC BY 4.0 License.



AEROSOL Research Discussions

2018). The field of view was centered approximately 3 cm downstream of the atomizer outlet, with spatial calibrations of 5.32 µm/px for Injector 1 and 13.957 µm/px for Injector 2.

Multiple recordings were acquired for each injector and voltage. For Injector 1, four recordings were analyzed at each voltage except 10 kV, for which three were available, and for Injector 2, three at each voltage except 6 kV, for which five were available. The resulting 50 recordings constitute the experimental dataset used in the subsequent analyses.

Because the recordings were acquired from a single viewing direction, the reconstructed trajectories and velocities represent only the motion projected onto the imaging plane. Furthermore, out-of-plane motion may affect focus, contour definition, and trajectory continuity, while partial overlaps and nonuniform illumination can influence segmentation and tracking.

Table 1. Geometrical parameters, operating conditions, imaging parameters, and fluid properties used in the electrically assisted Flow Blurring experiments. Liquid properties are given at ambient conditions; the reported gas density is the value used in the pneumatic reference calculations.

Parameter	Symbol	Injector 1	Injector 2
Discharge orifice diameter (nominal)	D	700 µm	900 µm
Tube-to-orifice gap (nominal)	H	50 µm	50 µm
Aspect ratio	H/D	0.0714	0.0556
Liquid	–	Type II water	
Liquid density	ρ_l	997 kg/m³	
Liquid dynamic viscosity	μ_l	8.9×10^{-4} Pa·s	
Liquid surface tension	σ_l	0.072 N/m	
Gas	–	Compressed air	
Gas density used in scaling	ρ_g	1.20 kg/m³	
Liquid flow rate	Q_l	4.062 mL/min	19.722 mL/min
Reported gas flow rate	Q_g	0.8047 L/min	2.33 L/min
Gas-to-liquid mass ratio	GLR	0.2384	0.1422
Inferred gas pressure difference	ΔP	9.04 kPa	47.10 kPa
Electrical conductivity of Type II water	κ_l	≈ 2.2 µS/cm	
Applied voltage	V	0–12 kV	
Acquisition rate	f_{acq}	10^6 fps	
Spatial calibration	s	5.32 µm/px	13.957 µm/px
Axial position of field-of-view center	x_{FOV}	≈ 3 cm	
Analyzed recordings per condition		3–4	3–5

https://doi.org/10.5194/ar-2026-52
Preprint. Discussion started: 24 November 2026
© Author(s) 2026. CC BY 4.0 License.

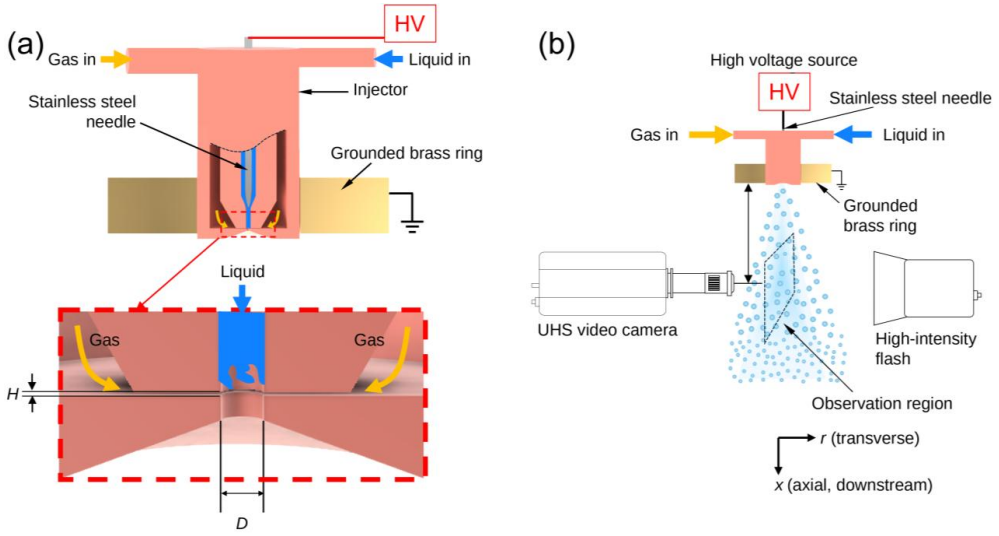

Figure 4. Experimental configuration for electrically assisted Flow Blurring atomization and UHS imaging. (a) Schematic of the electrically assisted Flow Blurring atomizer. The lower inset provides an enlarged view of the discharge region, and (b) side-view arrangement used for backlit visualization of the spray.

2.3.3. Video processing and data preparation

All recordings were processed directly with DA using the methodology described in Sect. 2.1, without external preprocessing. The same processing parameters were applied to all recordings from each injector, independent of V. The resulting droplet measurements, including equivalent diameter, centroid position, and velocity components, were converted to physical units using the corresponding spatial calibration and acquisition rate.

The reconstructed trajectories were subsequently screened to reduce the contribution of spurious detections and unreliable measurements. The screening criteria included the exclusion of single-frame trajectories, nearly stationary droplets (using a minimum trajectory speed of 1 m/s), and trajectories exhibiting physically implausible velocities or motion directions. Additional quality screening considered trajectory continuity and droplet morphology, with particular attention to short trajectories and irregular droplet contours. Further details are provided in Supplementary Sect. S2 and Table S4.

The processed datasets contained 3516 and 11138 trajectories for Injectors 1 and 2, respectively. For the spatial analysis, the transverse position of each trajectory was expressed using the normalized coordinate $\xi = |r|/D$, where $|r|$ is the absolute transverse distance from the spray axis and D is the nominal discharge orifice diameter. The analysis was restricted to $0 \leq \xi \leq 0.5$, divided into five non-overlapping intervals: [0, 0.1), [0.1, 0.2), [0.2, 0.3), [0.3, 0.4), and [0.4, 0.5], with the upper boundary included in the final interval. The final analysis included 1254 trajectories (35.7% of the processed dataset) for Injector 1 and 1954 (17.5%) for Injector 2, yielding 3208 trajectories distributed across 70 groups defined by injector, applied voltage, and transverse position. The selected trajectories were matched to their original recording and track identifiers to preserve data traceability. The smallest equivalent diameter retained in the analyzed trajectories is 6.18 px (projected area of 30 px^2), which corresponds to 32.9 µm for Injector 1 and 86.3 µm for Injector 2. Droplets below this size are therefore not represented in the statistics, which limits the interpretation of the lower end of the size distributions (Sect. 3.3.5).

https://doi.org/10.5194/ar-2026-52
Preprint. Discussion started: 24 November 2026
© Author(s) 2026. CC BY 4.0 License.



AEROSOL Research Discussions

For each injector–voltage–transverse-region group, two characteristic droplet diameters were calculated. The Sauter mean diameter, D_{32}, was obtained as the ratio of the third to the second moments of the number-based droplet size distribution:

$$D_{32} = \frac{\Sigma_i D_i^3}{\Sigma_i D_i^2}, \quad (8)$$

where D_i is the representative equivalent diameter of reconstructed droplet i. Each trajectory contributed one diameter, regardless of the number of frames over which the droplet was detected, preventing longer tracks from receiving greater statistical weight.

The volume median diameter, D_{v50}, was calculated directly from the empirical volume-weighted distribution. After sorting the diameters in ascending order, the cumulative volume fraction was calculated as

$$F_v(D_k) = (\Sigma_{i=1}^{k} D_i^3) \,/\, (\Sigma_{i=1}^{N} D_i^3). \quad (9)$$

D_{v50} was defined as the smallest diameter satisfying $F_v(D_k) \geq 0.5$. Both characteristic diameters were also calculated separately for independent recordings to assess experimental variability (Table S7).

The number median diameter, D_{n50}, and the 90th percentile, D_{n90}, were calculated from the representative equivalent diameters using linear interpolation between adjacent ordered values. For voltage-dependent analysis, the variation between independent recordings was characterized by the standard deviation of D_{v50}/D calculated separately for each recording. The spatial distribution of droplet diameters and the relationship between droplet size and velocity were examined using the same 3208 reconstructed trajectories. For each tracked droplet, a representative equivalent diameter and a median velocity were obtained from the corresponding measurements to ensure consistency between the spatial and kinematic analyses. Velocity estimates obtained from trajectories spanning only two frames were retained, although they are more sensitive to uncertainties in droplet position.

2.3.4. Reference pneumatic Flow Blurring scaling laws

To set the local droplet size measurements within the characteristic scales expected for conventional FB, two previously reported scaling expressions were evaluated and used as pneumatic reference scales.

The first relationship is the correlation proposed by Gañán-Calvo (2005) for the characteristic mass-median droplet diameter, denoted here as D_{FB}. Normalizing this diameter by the discharge orifice diameter, D, gives the dimensionless characteristic diameter δ_{FB}:

$$\delta_{FB} = \frac{D_{FB}}{D} = 0.42\,We_D^{-0.6}\,(1 + 18\,Oh_D)\,(1 + GLR^{-1})^{1.2} \quad (10)$$

where

$$We_D = \frac{\rho_g U_g^2 D}{2\sigma}, \qquad Oh_D = \frac{\mu_l}{\sqrt{\rho_l \sigma_l D}}, \qquad GLR = \frac{\dot{m}_g}{\dot{m}_l}. \quad (11)$$

Here, ρ_g and U_g are the gas density and velocity at the characteristic gas passage as defined by Gañán-Calvo (2005), ρ_l and μ_l are the liquid density and dynamic viscosity, and σ_l is the liquid surface tension. For a liquid of uniform density, the mass-median and volume-median diameters coincide. The characteristic diameter predicted by the pneumatic correlation, $D_{FB} = D\delta_{FB}$, can therefore be compared with the measured D_{v50} values. For both injectors, the characteristic gas passage was taken as the lateral cylindrical passage (LCP; Gañán-Calvo, 2005), with area $A_{LCP} = \pi DH$.

The gas mass flow rate was calculated from the volumetric flow rate at reference conditions as $\dot{m}_g = \rho_g Q_g$, using $\rho_g = 1.2$ kg m^{-3}. To estimate the characteristic gas conditions at the LCP, air was modeled as an ideal gas undergoing isentropic expansion from

https://doi.org/10.5194/ar-2026-52
Preprint. Discussion started: 24 November 2026
© Author(s) 2026. CC BY 4.0 License.



a stagnation temperature of T_0=296.15 K to a nominal static pressure equal to ambient pressure, P_a=101325 Pa. Note that the resulting gas velocity and density are therefore model estimates and not direct, local measurements.

The second pneumatic reference is the lower-envelope scaling relationship proposed by Rosell-Llompart and Gañán-Calvo (2008):

$$d_{FB,min}=1.42\, d_0 (Q_l/Q_0)^{1/5} \qquad (12)$$

where d_0 and Q_0 are the characteristic length and liquid flow rate, respectively, defined as

$$d_0=\frac{\sigma}{\Delta P}, \qquad Q_0=\left(\frac{\sigma_l^4}{\rho_l \Delta P^3}\right)^{1/2}, \qquad (13)$$

Here, d_0 is a characteristic capillary length obtained from the balance between surface tension and the available pressure difference, ΔP, while Q_0 is the corresponding characteristic liquid flow rate defined by the scaling relation. The resulting $d_{FB,min}$ should be interpreted as a lower-envelope estimate of the volume median droplet diameter under pneumatic atomization conditions.

Equations (10) and (12) are employed as fixed pneumatic reference scales in the subsequent analysis. The LCP-based reference calculations are documented in Supplementary Sect. S3 and Table S5.

3. Results and Discussion

3.1. Quantitative validation using synthetic video sequences

3.1.1. Segmentation accuracy (E1)

Static synthetic droplets with seven prescribed ground-truth diameters (6, 10, 15, 20, 30, 40, and 50 px) were analyzed under noise-free conditions to isolate the errors associated with segmentation and equivalent-diameter estimation. All droplets were correctly detected over the complete diameter range, with precision, recall, and F1-score equal to 1.00 in every case.

The detected equivalent diameter exhibited a small positive bias of 0.6–0.9 px over the complete range, without a systematic dependence on droplet size. Consequently, MRE_d decreased with increasing d_{GT}, from 9.7% at d_{GT} = 6 px to 1.4% at d_{GT} = 50 px, whereas $RMSE_d$ remained between 0.58 and 0.88 px. A bias of this magnitude is consistent with part of the blurred edge transition of each silhouette being assigned to the droplet by the adaptive threshold.

A representative subset of four diameters spanning the tested range is reported in Table 2. The diameter-dependent sizing errors and biases obtained in E1 and E4 are compared in Figs. 5a and 5b, while Fig. 5c presents the corresponding detection performance evaluated in E4 (Sect. 3.1.4). These results distinguish the ability to detect individual droplets from the accuracy of their diameter measurements.

Table 2. Segmentation and equivalent diameter accuracy for static synthetic droplets under noise-free conditions (E1).

d_{GT} (px)	Recall	Precision	MRE_d (%)	$RMSE_d$ (px)
6	1.00	1.00	9.7	0.58
15	1.00	1.00	5.9	0.88
30	1.00	1.00	2.9	0.86
50	1.00	1.00	1.4	0.71

https://doi.org/10.5194/ar-2026-52
Preprint. Discussion started: 24 November 2026
© Author(s) 2026. CC BY 4.0 License.



3.1.2. Velocity-estimation accuracy (E2)

A single synthetic droplet with a diameter of 20 px was tracked under nine prescribed velocity vectors with magnitudes from 0.2 to 5 px/frame, without noise and with Gaussian noise ($\sigma = 8$). All detections were correctly matched (F1 = 1.00), and each sequence was reconstructed as a single track.

For displacements of a whole number of pixels per frame without noise, the velocity was recovered exactly (Table 3), because the droplet image, and hence its segmented contour and centroid, is simply translated between frames; these cases verify the velocity-reconstruction procedure (association, finite differences, and unit handling) but not the localization accuracy. Sub-pixel displacements and image noise introduce frame-to-frame fluctuations of the centroid, and the standard deviation of the frame-to-frame velocity magnitude was 0.02–0.07 px/frame in all other cases. Because this absolute uncertainty is nearly independent of the droplet speed, the relative error depends mainly on the displacement per frame: MRE_v remained below 2.4% for velocities of about 1.5 px/frame and above, but increased to 10–20% for 0.4 and 0.2 px/frame. The track-averaged velocity was unbiased in all cases (within 0.005 px/frame of the prescribed value), indicating that the larger relative errors at low speeds primarily affect individual frame-to-frame estimates rather than track-averaged values. These results highlight the sensitivity of velocity measurements to small interframe displacements and support the screening of nearly stationary trajectories in the experimental analysis (Sect. 2.3.3 and Supplementary Sect. S2). The minimum-speed threshold of 1 m/s was adopted as a practical screening criterion rather than as a validated lower bound for velocity accuracy. E2 considers an isolated droplet and should not be interpreted as representative of tracking accuracy in dense sprays, which is examined in E5.

Table 3. Accuracy of the velocity magnitude estimates for nine prescribed droplet motions without noise and with Gaussian noise of $\sigma = 8$ (E2). The synthetic droplet diameter was 20 px. v_{det} is the mean ± standard deviation of the frame-to-frame velocity magnitude along the track.

(v_x, v_y) (px/frame)	v_{GT} (px/frame)	v_{det}, $\sigma = 0$ (px/frame)	MRE_v, $\sigma = 0$ (%)	v_{det}, $\sigma = 8$ (px/frame)	MRE_v, $\sigma = 8$ (%)
(2, 0)	2.000	2.000 ± 0.000	0.00	2.002 ± 0.056	2.22
(5, 0)	5.000	5.000 ± 0.000	0.00	5.001 ± 0.061	0.97
(0, 3)	3.000	3.000 ± 0.000	0.00	3.002 ± 0.041	1.01
(3, 3)	4.243	4.243 ± 0.000	0.00	4.244 ± 0.046	0.85
(−4, 2)	4.472	4.472 ± 0.000	0.00	4.474 ± 0.060	1.10
(1.3, 0.7)	1.476	1.478 ± 0.021	1.18	1.480 ± 0.045	2.34
(4.25, −1.6)	4.541	4.541 ± 0.044	0.75	4.541 ± 0.074	1.36
(0.4, 0)	0.400	0.399 ± 0.063	15.05	0.405 ± 0.048	9.78
(0.2, 0)	0.200	0.199 ± 0.043	16.32	0.205 ± 0.048	20.10

3.1.3. Noise robustness (E3)

The robustness of the framework to image degradation was evaluated using Gaussian noise with $\sigma \in \{0, 5, 10, 20, 35, 50\}$ and salt-and-pepper noise affecting 0–10% of the pixels (Table 4). The corresponding precision and recall values are presented in Figs. 5d and 5e, respectively. Detection was perfect (F1 = 1.00) up to $\sigma = 20$ and over the complete salt-and-pepper range. At $\sigma = 35$ and 50, the droplet was still detected in 97.5% of the frames, but the noise generated spurious objects that passed the area and circularity filters, reducing precision to 0.91 and 0.81 and the F1-score to 0.94 and 0.89, respectively.

https://doi.org/10.5194/ar-2026-52
Preprint. Discussion started: 24 November 2026
© Author(s) 2026. CC BY 4.0 License.



The equivalent-diameter bias increased moderately with Gaussian noise, from 0.87 px at σ = 0 to 1.8 px at σ = 20 and 1.5 px at σ = 50, so that MRE_d remained below 9%. Salt-and-pepper noise did not increase the sizing error; the bias decreased slightly, from 0.87 to 0.47 px, as the fraction of corrupted pixels increased.

These results reveal a trade-off governed mainly by the contour filters: the minimum projected area (15 px^2) and minimum circularity (0.5) selected on the tuning set suppress noise-induced objects up to moderate noise levels while preserving droplets down to about 4 px in diameter (E4). Stricter filters would be expected to improve precision at the highest noise levels at the expense of the smallest detectable droplet size.

All validation experiments used the same processing configuration, selected beforehand on the independent tuning set described in Sect. 2.2; no parameter was adjusted between or within experiments. The complete parameter set, including the settings fixed in the implementation, is given in Supplementary Table S1.

Table 4. Detection and equivalent-diameter accuracy for a static synthetic droplet of d_{GT} = 20 px under image-noise degradation (E3). The same processing configuration was used in E1–E5 (Supplementary Table S1).

Noise type	Level	F1-score	MRE_d (%)	$RMSE_d$ (px)
Gaussian	σ = 0	1.00	4.3	0.87
Gaussian	σ = 20	1.00	8.9	1.78
Gaussian	σ = 50	0.89	7.6	1.54
Salt-and-pepper	2%	1.00	4.0	0.79
Salt-and-pepper	10%	1.00	2.4	0.51

3.1.4. Detectable size range (E4)

The detectable size range of the framework was evaluated using synthetic videos containing a single centered droplet with prescribed diameters $d_{GT} \in \{3, 4, 5, 6, 8, 10, 12, 15, 20, 25, 30, 40, 50, 60, 70, 80\}$ px under additive Gaussian noise with $\sigma = 8$. This moderate synthetic-noise level was selected to provide a controlled degraded-image condition representative of the type of noise encountered in UHS recordings, rather than as a camera-calibrated noise measurement. The common processing configuration (Supplementary Table S1) was used throughout the diameter sweep.

Precision was 1.00 throughout the sweep (Table 5; Fig. 5c). All droplets with $d_{GT} \geq 4$ px were detected in every frame (recall = 1.00), whereas the 3 px droplet was detected in 70% of the frames (F1 = 0.82). The lower detection limit is set mainly by the minimum projected area of 15 px^2, which corresponds to an equivalent diameter of 4.4 px; the small positive sizing bias raises the apparent area of slightly smaller droplets above this threshold in some frames.

Equivalent-diameter accuracy exhibited a strong size dependence in relative terms. MRE_d decreased from about 48% for $d_{GT} \leq 4$ px to 1.0% at d_{GT} = 80 px, whereas the absolute error remained small, with $RMSE_d$ between 0.84 and 1.95 px over the investigated range and below 1.25 px for $d_{GT} \geq 12$ px. The relative sizing error fell below 10% for $d_{GT} \geq 15$ px and below 5% for $d_{GT} \geq 25$ px (Fig. 5a, b).

The results therefore define two distinct practical limits, that is, a detection limit and a more restrictive quantitative-sizing limit. DA can detect droplets approaching the image-resolution limit, whereas reliable quantitative sizing requires a substantially larger projected diameter. The corresponding error thresholds are specific to the present processing configuration and synthetic edge profile and should not be interpreted as universal limits of DA.

The pixel-based limits obtained in E4 should not be transferred directly to the experimental recordings as fixed physical diameter cutoffs. The experimental recordings of Sect. 3.3 were acquired at different spatial calibrations (5.32 µm px^{-1} for injector 1 and 13.957 µm px^{-1} for injector 2), so droplets of the same physical diameter are represented by different numbers

https://doi.org/10.5194/ar-2026-52
Preprint. Discussion started: 24 November 2026
© Author(s) 2026. CC BY 4.0 License.



of pixels in the two datasets. Moreover, the E4 thresholds depend on the synthetic edge profile and on the processing configuration used for validation. They are therefore used to identify the expected direction of resolution-related bias rather than to define a universal minimum measurable diameter. In particular, the lower spatial resolution of injector 2 can reduce sensitivity to the smallest droplets and may bias volume-weighted characteristic diameters toward larger values; similarly, any voltage-induced shift toward smaller droplets may be underestimated as droplets approach the effective detection limit. Comparisons between the two injector geometries are consequently interpreted with this limitation in mind. For reference only, the 4.4 px minimum-area equivalent from E4 corresponds to approximately 23 and 61 µm at the spatial calibrations of Injectors 1 and 2, respectively, while 15 px corresponds to approximately 80 and 209 µm. Likewise, a 1–2 px diameter bias would correspond nominally to about 5–11 µm for Injector 1 and 14–28 µm for Injector 2. These conversions illustrate the difference in physical resolution between the two imaging configurations; they are not experimental detection or sizing thresholds.

Table 5. Detection and equivalent-diameter accuracy for a single synthetic droplet under Gaussian noise (σ = 8) across the investigated range of ground-truth diameters (E4). Precision was 1.00 in all cases and is omitted.

d_{GT} (px)	Recall	F1-score	MRE_d (%)	$RMSE_d$ (px)
3	0.70	0.82	47.5	1.43
5	1.00	1.00	30.6	1.53
10	1.00	1.00	15.0	1.50
20	1.00	1.00	5.9	1.17
30	1.00	1.00	3.3	0.99
50	1.00	1.00	1.8	0.88
80	1.00	1.00	1.0	0.84

3.1.5. Multi-droplet tracking under increasing scene density (E5)

The effect of scene density on tracking performance was evaluated using synthetic sequences containing 5 to 50 simultaneously moving droplets (Table 6; Fig. 5f). Precision remained 1.00 in all cases. As the number of droplets increased, recall decreased from 1.00 to 0.82 and the F1-score from 1.00 to 0.90, consistent with overlapping droplets being merged into single objects that are either rejected by the shape filters or matched to only one of the overlapping ground-truth droplets. The velocity error increased from MRE_v = 2.1% to 10.3%.

Tracking deterioration became particularly evident at the highest scene densities, indicating that correct frame-to-frame association becomes progressively more difficult as droplet encounters and trajectory intersections increase.

Trajectory continuity was more sensitive to density than detection. Each ground-truth droplet was represented by a single track for $N_d = 5$, but by 1.7 tracks on average for $N_d = 20$ and 2.4 tracks for $N_d = 50$, with 14 and 70 identity switches, respectively. The track-count deviation Δ_{tracks} increased monotonically from 0 to 0.52 but underestimates this degradation, because it does not account for tracks that switch between droplets. The increase in velocity error at the highest densities is consistent with incorrect frame-to-frame associations, rather than segmentation alone, becoming an important source of uncertainty under crowded conditions.

This experiment represents a deliberately demanding tracking scenario because droplets move in randomly assigned directions, thereby promoting trajectory intersections and spatial occlusions. The same segmentation and tracking configuration was retained throughout the density sweep so that the observed changes reflect increasing scene complexity rather than parameter retuning. When synthetic droplets overlap, segmentation and subsequent association may both contribute to tracking errors. Actual atomization images generally exhibit a preferential downstream motion imposed by the mean spray flow, which may

https://doi.org/10.5194/ar-2026-52
Preprint. Discussion started: 24 November 2026
© Author(s) 2026. CC BY 4.0 License.

reduce the frequency of such crossings. Local turbulent fluctuations, out-of-plane motion, droplet overlap, and spatially varying concentration can nevertheless produce substantial association errors in experimental recordings.

The E5 results should therefore be interpreted as a controlled stress test of the tracking algorithm rather than as a direct quantitative estimate of tracking uncertainty in real sprays.

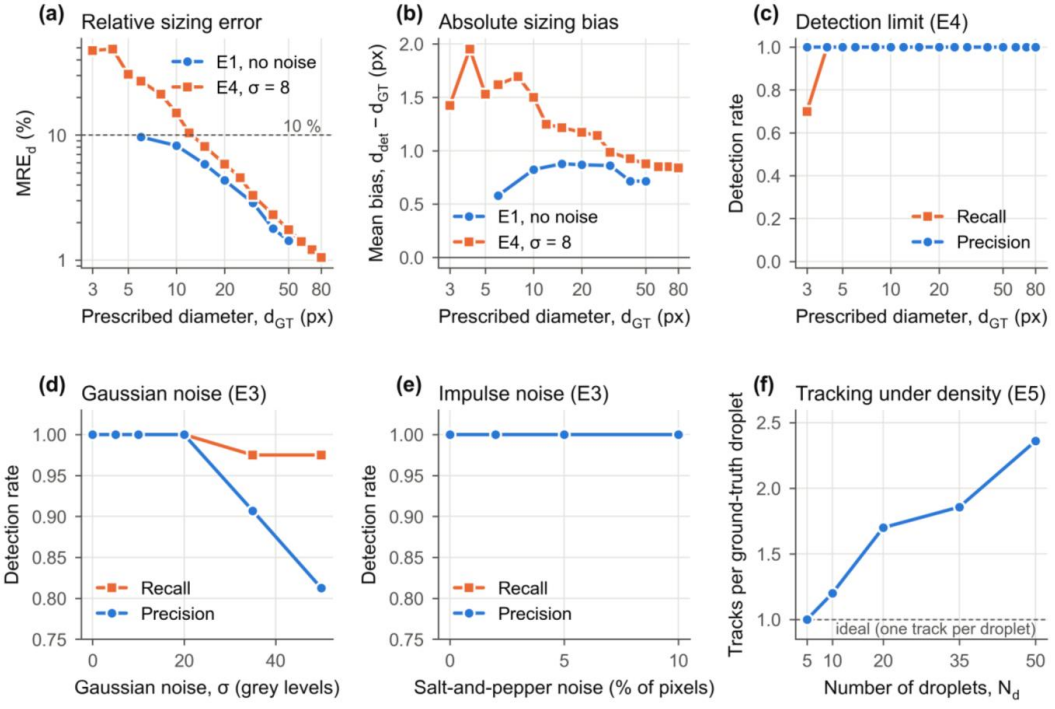

Figure 5. Summary of the quantitative validation of DA using synthetic sequences, all processed with the same configuration. (a) Mean relative error and (b) mean signed bias of the equivalent diameter as functions of the prescribed diameter, without noise (E1) and with Gaussian noise σ = 8 (E4); (c) precision and recall as functions of droplet size (E4); (d, e) precision and recall under Gaussian and salt-and-pepper noise (E3; both equal 1.00 throughout panel e); (f) mean number of reconstructed tracks per ground-truth droplet as a function of the number of simultaneously moving droplets (E5).

Table 6. Tracking performance as a function of the number of simultaneously moving synthetic droplets (E5). d_{GT} = 18 px, v_{GT} = 3 px/frame, and Gaussian noise with σ = 8.

Number of droplets, N_d	Recall	F1-score	Tracks per GT droplet	MRE_v (%)
5	1.00	1.00	1.00	2.1
10	0.96	0.98	1.20	3.4
20	0.90	0.95	1.70	7.4
35	0.89	0.94	1.86	7.9
50	0.82	0.90	2.36	10.3

3.1.6. Computational performance

Processing speed was measured on a desktop computer with an Intel Core i7-9700F CPU (3.0 GHz) and OpenCV 4.12, using the configuration of Supplementary Table S1 and timing each stage of the pipeline separately (Table S3). For the three

https://doi.org/10.5194/ar-2026-52
Preprint. Discussion started: 24 November 2026
© Author(s) 2026. CC BY 4.0 License.



experimental HPV-2 recordings analyzed (312 × 260 px, 102 frames each), DA processed 9.1 fps (110 ms per frame), that is, about 11 s per recording; for the 512 × 512 px synthetic sequences, the rate was 5.7–5.9 fps. Preprocessing, dominated by Non-Local Means denoising, accounted for 96–99% of the processing time, whereas thresholding and morphology, contour extraction and feature computation, and tracking together accounted for less than 4%. Because the OpenCV implementation of this filter did not benefit from additional threads in our tests, the processing rate was the same with one or eight threads. Processing time increased with image size in the present tests and was dominated by the Non-Local Means denoising stage; it could be reduced substantially by using a lighter denoising filter or by restricting the analysis to a region of interest, at the expense of the noise robustness characterized in E3.

3.2. Benchmark against previously published high-pressure measurements

To further evaluate its performance, Droplet Analyzer was compared with previously published experimental measurements of droplet size. The reference case corresponds to the Flow Blurring atomization of water under high-pressure conditions reported by Modesto-López and Gañán-Calvo (2018), at $\Delta P = 200$ kPa, $Q_l = 5$ mL/min, and gas-inlet pressure $P_o = 3.2$ MPa, corresponding to a chamber pressure P_i of 3.0 MPa (Fig. 5c of Modesto-López and Gañán-Calvo, 2018). The original study reported volume-based droplet size distributions measured using Malvern Spraytec laser diffraction and Automated Droplet Measurement (ADM), an image-analysis method introduced by Chong et al. (2016). ADM was originally developed for automated droplet measurements in microfluidic systems, where droplet generation and imaging conditions are generally more controlled than in dense atomization sprays. Its application to Flow Blurring measurements therefore provides a useful comparison with DA, which was developed to analyze multiple droplets and reconstruct their trajectories in high-speed spray recordings.

Four independent HS videos corresponding to the same operating condition, as in the original report of Modesto-López and Gañán-Calvo (2018), were processed with DA following the pipeline described in Sect. 2.1. The same segmentation parameters were applied to all four recordings to ensure consistency across measurements. For each video, a lognormal distribution was fitted to the resulting volume-weighted droplet size data. The original experiments used a horizontal field of view of 1.4 mm, corresponding to a spatial calibration of approximately 4.49 µm px^{-1} for the 312-pixel-wide HPV-2 images. At this resolution, droplets with diameters of 30–40 µm occupy approximately 7–9 pixels, making their measured diameters sensitive to contour detection, as discussed in Sect. 3.1.4.

Figure 6 compares the four lognormal distributions obtained with DA with the Spraytec and ADM measurements reported under the same operating conditions. The comparison focuses on characteristic droplet size and distribution shape. The secondary Spraytec peak at approximately 2–3 µm falls below the size range resolved by the high-speed images and is therefore not represented in the image-based measurements. At the nominal spatial calibration, the minimum projected-area criterion of 15 px^2 corresponds to an equivalent diameter of approximately 4.4 px (20 µm). However, the synthetic validation showed that sizing accuracy decreases as droplet diameter approaches the resolution limit. This reduced sensitivity to small droplets may affect the resulting size distributions and their characteristic diameters.

https://doi.org/10.5194/ar-2026-52
Preprint. Discussion started: 24 November 2026
© Author(s) 2026. CC BY 4.0 License.

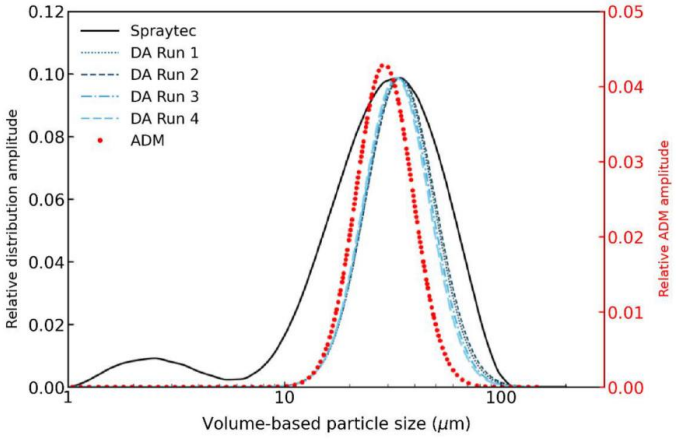

Figure 6. Volume-based droplet size distributions for Flow Blurring atomization of water at $\Delta P = 200$ kPa, $Q = 5$ mL/min, and gas-inlet pressure $P_o = 3.2$ MPa (chamber pressure $P_i \approx 3.0$ MPa). The black line and red symbols represent the Spraytec and ADM measurements, respectively, replotted from the original experimental data of Modesto-López and Gañán-Calvo (2018). The four blue curves represent lognormal fits to independent high-speed recordings analyzed with DA. The DA curves are peak-matched to the main Spraytec peak to facilitate comparison of characteristic droplet size and distribution shape, whereas the ADM measurements are displayed on a separately scaled right ordinate. Consequently, the plotted ordinates represent relative distribution amplitudes and should not be compared quantitatively among the three methods.

For this operating condition, Modesto-López and Gañán-Calvo (2018) reported a volume-based mean droplet diameter of 31.0 µm and a distribution standard deviation parameter of 0.803 from Spraytec measurements (Table 1 of the original study). The lognormal fit to the ADM measurements yielded a median diameter of 31.7 µm and a geometric standard deviation (GSD) of 1.3. The four independent DA measurements gave median diameters of 40.7, 38.5, 40.0, and 36.6 µm for Runs 1–4, respectively, with corresponding GSDs of 1.518, 1.522, 1.540, and 1.562.

The differences between the DA and ADM median diameters range from 4.9 to 9.0 µm, equivalent to approximately 1.1–2.0 pixels at the nominal spatial calibration. These differences are comparable to the positive sizing bias observed in the synthetic validation, suggesting that finite spatial resolution contributes to the observed offset. Segmentation, sampling, reduced sensitivity to smaller droplets, and differences in measurement principles may also contribute. Both the Spraytec and DA distributions extend toward larger droplet diameters approaching 100 µm, whereas ADM exhibits a narrower upper tail.

Beyond the agreement in characteristic droplet size, DA preserves the association between each detected droplet and its reconstructed trajectory, allowing droplet size, morphology, position, and velocity to be analyzed together. This capability extends the analysis from global size distributions to the spatial and kinematic characterization of individual droplets within the spray.

3.3. Application of Droplet Analyzer to electrically assisted Flow Blurring sprays

The experimental analysis combines droplet size, transverse position, and velocity measurements from 3208 trajectories described in Sect. 2.3.3. The results characterize the spatial distribution of droplet sizes and their response to applied voltage, together with the relationship between droplet size and velocity.

https://doi.org/10.5194/ar-2026-52
Preprint. Discussion started: 24 November 2026
© Author(s) 2026. CC BY 4.0 License.



3.3.1. Spatial discretization of the spray

The transverse position of each trajectory was determined relative to the spray axis using the mean lateral coordinate, r, measured in the imaging plane. This position was normalized by the D, to obtain, ξ, as defined in Sect. 2.3.3. The sampled spray was divided into five transverse regions:

$$Z_1 : 0.0 \leq \xi < 0.1$$
$$Z_2 : 0.1 \leq \xi < 0.2$$
$$Z_3 : 0.2 \leq \xi < 0.3$$
$$Z_4 : 0.3 \leq \xi < 0.4$$
$$Z_5 : 0.4 \leq \xi \leq 0.5$$

In the UHS images, the five transverse regions correspond to bands parallel to the spray axis. The same normalized intervals were used for both injectors and all applied voltages, allowing consistent spatial comparisons despite differences in optical magnification. Droplet size statistics were calculated separately for each injector, voltage, and transverse region. The representative position of each population was defined as the mean normalized transverse coordinate of its constituent trajectories:

$$\bar{\xi} = \frac{1}{N} \sum_{i=1}^{N} \frac{|r_i|}{D} \qquad (14)$$

Each local characteristic diameter was plotted at this representative position.

3.3.2. Local characteristic droplet diameters

Figure 7 presents the spatial variation of the Sauter mean diameter, D_{32}, and the volume median diameter, D_{v50}, for both injectors at applied voltages from 0 to 12 kV. To assess experimental variability, these diameters were also calculated separately for independent recording and transverse region. Table S7 reports the corresponding means and standard deviations, together with the number of recordings and trajectories contributing to each population.

The spatial distributions of D_{32} (Figs. 7a and 7b) exhibit considerable variations across sampled regions, including under conventional FB conditions (0 kV). Between 2 and 8 kV, the characteristic diameters show spatially dependent fluctuations relative to the zero-voltage values. At 10 kV, reductions become more apparent, particularly for Injector 1, while at 12 kV, D_{32} is lower than its zero-voltage value in all five transverse regions of both injectors. These reductions range from approximately 20% to 64% for Injector 1 and from 12% to 26% for Injector 2.

A similar response is observed for D_{v50} (Figs. 7c and 7d). At 0 kV, both injectors exhibit substantial spatial variations, with generally larger droplets near the spray axis for Injector 1. At intermediate voltages, the distributions remain variable, with no consistent progression as voltage increases. At 10 kV, D_{v50} decreases relative to 0 kV in most transverse regions, while at 12 kV all five regions exhibit smaller volume median diameters. These reductions at 12 kV range from approximately 26% to 71% for Injector 1 and from 24% to 49% for Injector 2. Thus, both characteristic diameters show a spatially consistent reduction at the highest applied voltage, with a generally stronger response for Injector 1.

The pneumatic reference diameters in Figs. 7c and 7d provide a basis for comparing the measurements with conventional FB atomization (Eqs. (10) and (12)) . At 0 kV, the local D_{v50} values range from 65.76 to 191.72 µm for Injector 1 and from 165.17 to 218.50 µm for Injector 2. At 12 kV, these ranges decrease to 48.40–61.79 µm and 107.97–131.76 µm, respectively. For Injector 1, the values at 12 kV lie between the two pneumatic reference scales, $D\delta_{FB}$ and $d_{FB,min}$, whereas those of Injector 2 are close to $D\delta_{FB}$. The $d_{FB,min}$ for Injector 2 (15.81 µm) lies below the minimum diameter represented in the experimental measurements (86.3 µm), limiting the interpretation of this reference for that injector.

https://doi.org/10.5194/ar-2026-52
Preprint. Discussion started: 24 November 2026
© Author(s) 2026. CC BY 4.0 License.



AEROSOL Research Discussions

Overall, the spatially resolved measurements reveal a voltage-dependent response that becomes particularly consistent at 12 kV. The reduction in both D_{32} and D_{v50} across all sampled regions is consistent with an increasing contribution of electrical forcing to the atomization process. Possible contributions include electrically induced liquid deformation, droplet charging, and subsequent droplet transport. The measured net electrical current and its relationship with the Sauter mean diameter are examined in Supplementary Sects. S5.2 and S5.3.

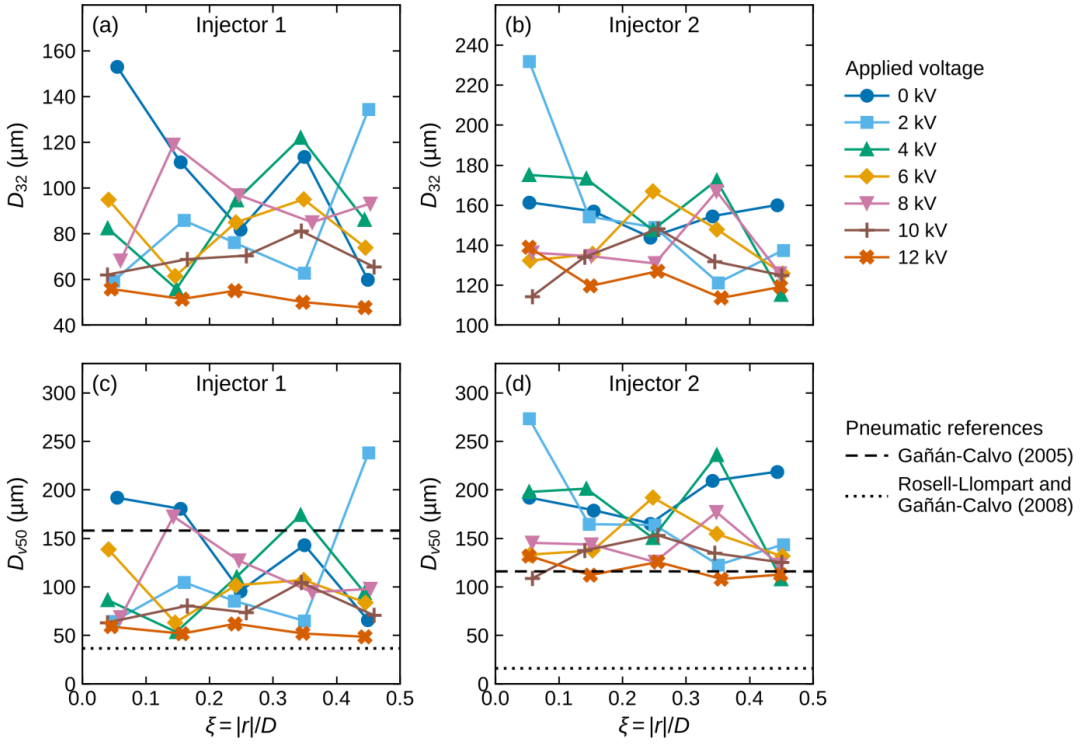

Figure 7. Spatially resolved characteristic droplet diameters in electrically assisted Flow Blurring sprays. The Sauter mean diameter, D_{32} , is shown for (a) Injector 1 and (b) Injector 2, while the volume-median diameter, D_{v50}, is shown for (c) Injector 1 and (d) Injector 2. Measurements are plotted as a function of the normalized transverse position, $\xi = |r|/D$, for applied voltages of 0–12 kV. Each symbol represents the characteristic diameter calculated from corresponding injector–voltage–transverse region population. In panels (c) and (d), horizontal dashed lines indicate the pneumatic characteristic diameters from Eq. (10) while dotted lines indicate the lower-envelope scales from Eq. (12). Those diameters are $D\delta_{FB}$ = 157.93 µm and $d_{FB,min}$ = 36.58 µm for Injector 1, and $D\delta_{FB}$ = 116.11 µm and $d_{FB,min}$ = 15.81 µm for Injector 2. Lines connecting experimental symbols are included only as visual guides.

3.3.3. Number-based and volume-based response to applied voltage

Figure 8 depicts the voltage dependence of the volume-based and number-based droplet diameters for both injectors, calculated from the trajectories within the sampled transverse region. The data show that the normalized volume median diameter, D_{v50}/D, decreases at higher applied voltages (Fig. 8a). Between 0 and 12 kV, D_{v50}/D decreases from 0.204 to 0.077 for Injector 1 and from 0.203 to 0.130 for Injector 2, corresponding to reductions of 62.2% and 36.2%, respectively. At intermediate voltages, the response is nonuniform, particularly for Injector 1.

The number median diameter, D_{n50}, exhibits relatively small variations with applied voltage (Fig. 8b). In contrast, the 90th percentile of the number-based distribution, D_{n90}, decreases from approximately 0.140D to 0.088D for Injector 1 and from

https://doi.org/10.5194/ar-2026-52
Preprint. Discussion started: 24 November 2026
© Author(s) 2026. CC BY 4.0 License.



0.208D to 0.146D for Injector 2. Thus, these results indicate that the voltage-dependent variations are more pronounced in the upper portion of the droplet size distribution, particularly at 12 kV.

The combined response of the three characteristic diameters indicates that applied voltage primarily modifies the upper portion of the droplet size distribution. The substantial reduction in D_{v50}, together with the decrease in D_{n90} and the small variation in D_{n50}, suggests that the observed size reduction is associated mainly with a contribution from larger droplets, while the central part of the number-based distribution remains relatively stable. This distinction is particularly relevant because larger droplets contribute disproportionately to the total liquid volume.

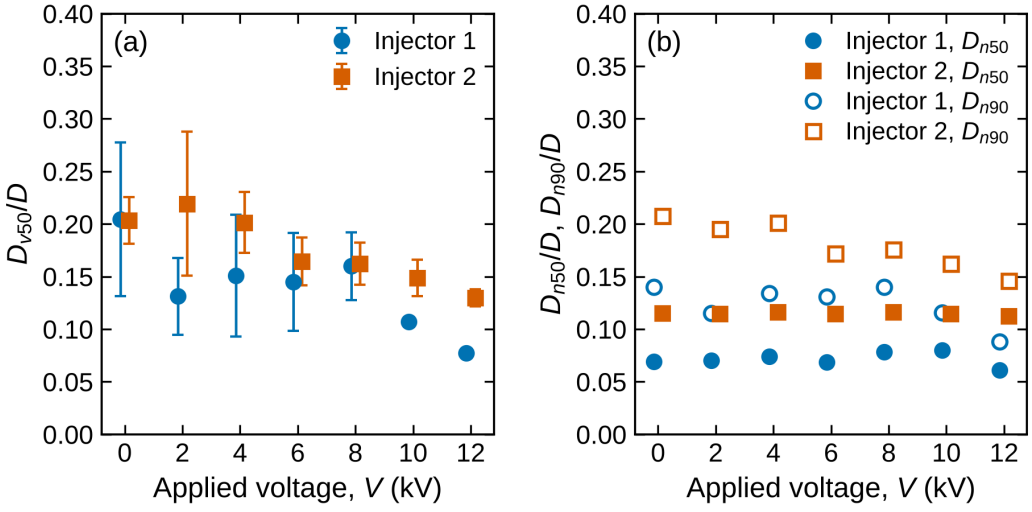

Figure 8. Voltage dependence of characteristic droplet diameters for Injector 1 (D = 700 µm) and Injector 2 (D = 900 µm), within $0 \leq \xi \leq 0.5$. (a) Volume median diameter normalized by the discharge-orifice diameter, D_{v50}/D. Error bars show the standard deviation of D_{v50}/D calculated from independent recordings at each operating condition; where not visible, error bars are smaller than the symbols. (b) Number median diameter, D_{n50}/D (filled symbols), and the 90th percentile of the number distribution, D_{n90}/D (open symbols).

3.3.4. Local response to applied voltage

The overall reduction in D_{v50} observed at high voltage (Sect. 3.3.3) was further examined across the sampled transverse regions. For each injector, the local volume median diameter was normalized by its corresponding value at 0 kV within the same region:

$$R_D(V,Z_j)=\frac{D_{v50}(V,Z_j)}{D_{v50}(0,Z_j)}, \qquad (15)$$

where Z_j is the j-th transverse region defined in Sect. 3.3.1. Values of R_D below unity indicate a reduction in the local volume median diameter relative to conventional FB (0 kV). The error bars for the 12 kV measurements represent the 95% intervals obtained by resampling recordings and then trajectories, following the procedure described in Supplementary Sect. S5.

Figure 9 shows R_D as a function of ξ. At 12 kV, all estimated local median diameter ratios are below unity, indicating a consistent reduction across the sampled transverse regions, although the sampling intervals include unity in some regions. For Injector 1, the largest reductions are observed in Z_1, Z_2, and Z_4, where R_D= 0.31, 0.29, and 0.36, respectively. The smallest

https://doi.org/10.5194/ar-2026-52
Preprint. Discussion started: 24 November 2026
© Author(s) 2026. CC BY 4.0 License.

reduction occurs in Z_5, where R_D= 0.74. For Injector 2, R_D ranges from 0.51 to 0.76, corresponding to reductions of 24.0% to 49%. The sampling intervals include unity in Z_3 and Z_5 for Injector 1 and in Z_1, Z_3-Z_5 for Injector 2, thus indicating greater uncertainty in the magnitude and direction of the response in these regions.

At intermediate voltages, R_D varies with transverse position without a clear trend as voltage increases. The value of 3.6 at 2 kV in Z_5 of Injector 1 is isolated and is not repeated at other voltages. The reduction at 12 kV is more pronounced for Injector 1, particularly in the inner transverse regions, whereas Injector 2 exhibits a smaller and more spatially uniform response.

These results indicate that applying 12 kV is associated with a reduction in the local median droplet diameter across the transverse regions of both injectors, although the magnitude of this reduction is not equally well resolved in all regions. The observed differences between injectors and across transverse positions suggest that the droplet size response to electrical forcing is influenced by the injector configuration and local spray conditions. The considerable variability at intermediate voltages further indicates that the relationship between applied voltage and droplet size is not straightforward, with the clearest evidence of a reduction occurring at the highest voltage.

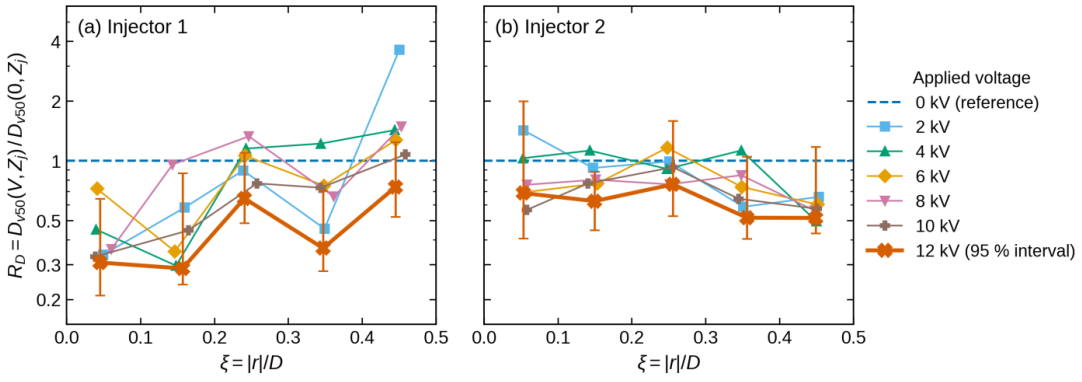

Figure 9. Spatial variation of the local volume median diameter ratio, R_D (Eq. 15), as a function of the normalized transverse position $\xi = |r|/D$ for (a) Injector 1 and (b) Injector 2. Each symbol is plotted at the mean position of the droplets in the corresponding transverse region. The thick line represents the response at 12 kV, with error bars indicating 95% sampling intervals calculated by resampling recordings and trajectories (Supplementary Sect. S5). Thin lines represent intermediate voltages (2–10 kV). The dashed horizontal line at R_D = 1 indicates equality with the zero-voltage reference. The vertical axis is logarithmic, and lines connect symbols to guide the eye.

3.3.5. Transverse distribution of droplet size quantiles

Figure 10 presents the transverse variation of the volume median diameter, D_{v50}, and the corresponding 10th and 90th volume percentiles, D_{v10} and D_{v90}, for both injectors. The comparison focuses on 0 and 12 kV, where the strongest and most consistent differences in droplet size were observed. The percentiles were calculated from the cumulative volume distribution (Eq. 9). The shaded bands between D_{v10} and D_{v90} contain the central 80% of the equivalent droplet volume in each transverse region, showing the spread of the local size distributions.

For Injector 1 (Fig. 10a), D_{v50} ranges from approximately 66 to 192 µm at 0 kV, indicating considerable differences in droplet size across the spray. At 12 kV, the median decreases to 48–62 µm, becoming nearly uniform across the five transverse regions. The D_{v10}–D_{v90} bands also shift toward smaller diameters and become narrower. Thus, at 12 kV, the reduction in droplet size is accompanied by smaller differences between regions and a narrower range of droplet sizes within each region. The narrowing

https://doi.org/10.5194/ar-2026-52
Preprint. Discussion started: 24 November 2026
© Author(s) 2026. CC BY 4.0 License.



arises mainly from the upper percentile, since D_{v10} converges to approximately 37–39 µm in all five regions, within about 1 px of the minimum diameter (32.9 µm), so the lower edge of the bands is limited by image resolution.

Injector 2 (Fig. 10b) shows a reduction in D_{v50}, from 165–219 µm at 0 kV to 108–132 µm at 12 kV. However, its upper volume percentiles remain relatively large, indicating that larger droplets continue to contribute appreciably to the measured volume. Moreover, considering all voltages, approximately 37.6% of the trajectories have diameters between 6.18 and 7 px and account for 13.1% of the equivalent droplet volume. Consequently, the measured D_{v10} values (approximately 90–101 µm) lie close to the minimum diameter (86.3 µm) and may be sensitive to image resolution and segmentation.

The main finding is that applied voltage modifies the median droplet size and the absolute spread of the local distributions, whereas the relative span shows no clear change (Supplementary Sect. S5.1). However, this response cannot be fully described by a single characteristic diameter, highlighting the value of spatially resolved size distributions.

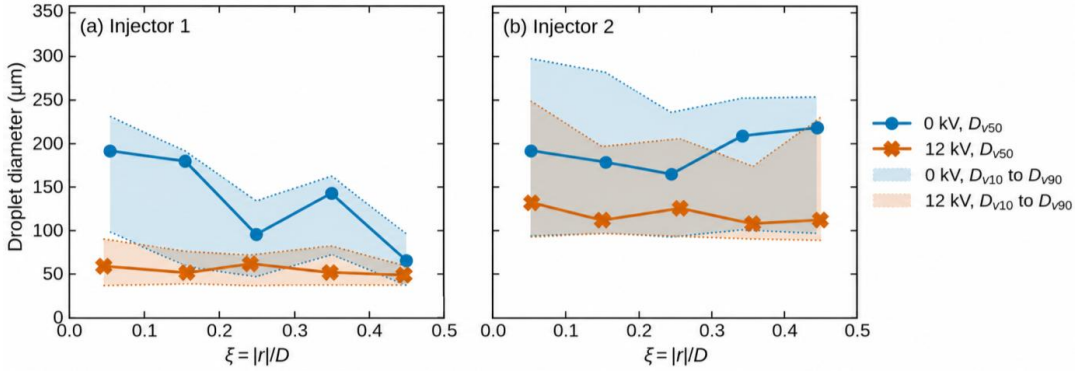

Figure 10. Transverse distributions of volume-based droplet size quantiles at 0 and 12 kV for (a) Injector 1 and (b) Injector 2. Symbols and lines represent the volume median diameter, D_{v50}, at 0 kV (blue) and 12 kV (orange). Shaded bands extend from D_{v10} to D_{v90} and contain the central 80% of the equivalent droplet volume in each transverse region. Quantiles were calculated from the cumulative volume distribution (Eq. 9). The shaded bands describe the spread of the local size distributions and do not represent uncertainty in the median. Symbols are plotted at the mean normalized transverse position of each population, and connecting lines serve as visual guides.

3.3.6. Droplet size and velocity

Figure 11 depicts the relationship between droplet diameter and velocity for both injectors. The trajectories between the 2nd and 98th diameter percentiles were grouped into ten diameter intervals, with the same interval boundaries used for all voltages. The colored curves represent the median velocity at each voltage for groups containing at least eight trajectories. The black line shows the median velocity across all voltages, while the gray band indicates the interquartile range (25th–75th percentiles).

Median droplet velocity generally decreases with increasing diameter, a trend that is particularly evident for Injector 2, where it drops from approximately 68 to 57 m s^{-1}, while Injector 1 follows a similar tendency with larger variation between voltage conditions. The relatively wide interquartile ranges indicate substantial velocity differences among droplets of similar diameter. Injector 2 exhibits higher velocities than Injector 1 despite its generally larger droplets, which indicates that droplet size alone does not explain the differences between the two configurations.

The observed size dependence is consistent with the influence of droplet inertia on aerodynamic acceleration, as larger droplets respond more slowly to changes in the surrounding gas velocity. For instance, for spherical droplets in the Stokes regime, the

https://doi.org/10.5194/ar-2026-52
Preprint. Discussion started: 24 November 2026
© Author(s) 2026. CC BY 4.0 License.

characteristic relaxation time is $\tau_p = \frac{\rho_l d^2}{18\mu_g}$, which increases with the square of the droplet diameter. For the investigated diameter range, this reference timescale is approximately 3–120 ms, considerably longer than the characteristic transit time across the observed field of view. This suggests that droplet velocities may retain a dependence on their previous acceleration history, particularly for larger droplets. However, the Stokes expression holds only when the Reynolds number based on the relative gas–droplet velocity is well below unity, which is unlikely for the larger droplets, and at higher Reynolds numbers the drag exceeds the Stokes value, so the actual relaxation time may be shorter than this estimate. Overall, differences in droplet inertia may contribute to the observed trend if droplets are still accelerating within the gas flow, while the considerable velocity scatter suggests that local flow conditions and individual droplet trajectories also influence the measured velocities.

Despite the reduction in characteristic droplet diameter at high voltage, velocity does not systematically change with applied voltage, as the velocity curves overlap and intersect across much of the measured diameter range. This behavior may partly reflect the electrode configuration, where the high-voltage needle and grounded ring generate a nonuniform electric field that could affect droplet formation near the injector without substantially altering droplet velocities farther downstream, where aerodynamic forces also influence their motion. Wang et al. (2014) reported a similar distinction between the effects of the electric field on droplet size and velocity in electrostatically assisted twin-fluid atomization. These results suggest that changes in droplet size and velocity do not necessarily follow the same response to applied voltage, highlighting the value of measuring both quantities along individual trajectories.

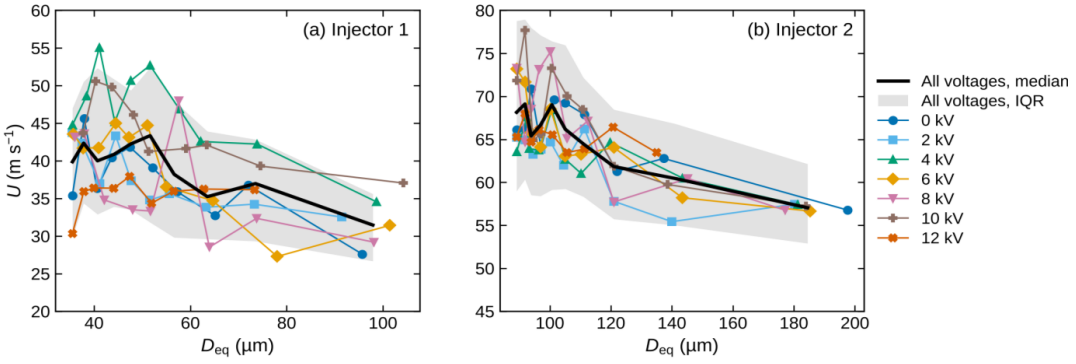

Figure 11. Relationship between droplet diameter and velocity for (a) Injector 1 and (b) Injector 2. The analysis includes 1206 and 1879 trajectories, respectively, selected between the 2nd and 98th percentiles of equivalent diameter from the original 1254 and 1954 trajectories. For each injector, droplets were grouped into ten diameter intervals defined by quantiles, using the same interval boundaries for all voltages. Colored symbols show the median trajectory velocity at each voltage for groups containing at least eight trajectories. The horizontal position of each symbol corresponds to the median equivalent diameter of its group. The black line shows the median velocity across all voltages, while the gray band represents the interquartile range (25th–75th percentiles). Lines connecting symbols serve as visual guides.

4. Conclusions

Droplet Analyzer (DA) is an automated, open-source framework based on OpenCV for measuring droplet size, morphology, position, and velocity from ultra-high-speed recordings. By combining droplet detection with trajectory reconstruction, DA enables these properties to be examined together for individual droplets, providing information on their spatial distributions and dynamics. The complete processing workflow was evaluated using a parameter configuration selected independently of the evaluation data.

Validation with synthetic image sequences established the performance of DA under controlled conditions. Droplets as small as 4 px were detected under moderate noise, while relative sizing errors remained below 10% for diameters of 15 px or larger. The measurements exhibited a positive diameter bias of approximately 1 px, largely independent of droplet size. For isolated

https://doi.org/10.5194/ar-2026-52
Preprint. Discussion started: 24 November 2026
© Author(s) 2026. CC BY 4.0 License.



droplets, velocity errors remained below 2.4% for displacements of approximately 1.5 px per frame or greater, whereas trajectory-averaged velocities showed no systematic bias even at subpixel displacements. Increasing droplet density primarily affected trajectory reconstruction, resulting in up to 2.4 reconstructed tracks per droplet at the highest density. Regarding computational performance, processing a 102-frame recording required approximately 11 s, with denoising accounting for most of the processing time.

Comparison with previously published Flow Blurring measurements provided an experimental benchmark. The median diameters obtained with DA were 1.1–2.0 px larger than those reported using an earlier image analysis method, consistent with the positive sizing bias identified in the synthetic validation. Furthermore, the DA distributions extended toward larger droplet diameters, in agreement with the upper size range measured by laser diffraction.

Application to electrically assisted Flow Blurring sprays demonstrated the ability of DA to characterize changes in droplet size across different voltage conditions and transverse positions. Analysis of 3208 trajectories revealed a variable response at intermediate voltages, followed by reductions in the local Sauter mean and volume median diameters at 12 kV across all five sampled regions of both injectors. The overall volume median diameter decreased by 62.2% for Injector 1 and 36.2% for Injector 2, while the number median diameter changed comparatively little. However, the simultaneous reduction in the 90th percentile of the number distribution indicates that the upper portion of the droplet size distribution was also affected. At 12 kV, the local volume median diameters became more uniform across the sampled transverse regions, particularly for Injector 1, although the two injectors exhibited different changes in their local size distributions.

Droplet velocity generally decreased with increasing diameter, consistent with the influence of droplet inertia on aerodynamic acceleration. However, despite the substantial reductions in characteristic droplet size at high voltage, the size-resolved velocity measurements showed no systematic dependence on applied voltage. These observations suggest that droplet size and velocity do not necessarily respond in the same way to electrical forcing. By allowing these properties to be examined together with droplet morphology and position along individual trajectories, DA provides a useful framework for investigating the relationships between droplet characteristics and dynamics in atomizing flows.

Code and data availability

The source code of Droplet Analyzer (v1.0.0), including the synthetic-video generator, evaluation scripts, and processing parameters used in this work, is available at https://github.com/carperca23/droplet-analyzer.

The trajectory-level data and Python scripts supporting the statistical analyses presented in this study are available from Zenodo (Pérez-Cantalapiedra et al., 2026, https://doi.org/10.5281/zenodo.24201211).

Author contributions

Carlos Pérez-Cantalapiedra: Conceptualization, Investigation, Software, Validation, Visualization, Formal analysis, Writing – review & editing. Manuel Carranza-García: Investigation, Software, Supervision, Writing – original draft, Writing – review & editing. Luis B. Modesto-López: Conceptualization, Funding acquisition, Investigation, Supervision, Project administration, Resources, Writing – original draft, Writing – review & editing.

Competing interests

The authors declare that they have no conflict of interest.

Disclaimer

https://doi.org/10.5194/ar-2026-52
Preprint. Discussion started: 24 November 2026
© Author(s) 2026. CC BY 4.0 License.



Copernicus Publications remains neutral with regard to jurisdictional claims made in the text, published maps, institutional affiliations, or any other geographical representation in this paper. While Copernicus Publications makes every effort to include appropriate place names, the final responsibility lies with the authors. Views expressed in the text are those of the authors and do not necessarily reflect the views of the publisher.

Financial support

L.B.M.L. acknowledges financial support from project PID2022-140951OB-C21 financed by MCIN/AEI/10.13039/501100011033.

M.C.G. acknowledges financial support from Grant PID2023-146037OB-C21 funded by MICIU/AEI/10.13039/501100011033.

Acknowledgements

The authors used AI tools to assist in developing the Python scripts for data analysis and figure preparation. All code and results were verified by the authors, who take full responsibility for the content of this article.

References

Basu, A. S.: Droplet morphometry and velocimetry (DMV): a video processing software for time-resolved, label-free tracking of droplet parameters, Lab Chip, 13, 1892–1901, https://doi.org/10.1039/C3LC50074H, 2013.

Bothell, J. K., Machicoane, N., Li, D., Morgan, T. B., Aliseda, A., Kastengren, A. L., and Heindel, T. J.: Comparison of X-ray and optical measurements in the near-field of an optically dense coaxial air-assisted atomizer, Int. J. Multiph. Flow, 125, 103219, https://doi.org/10.1016/j.ijmultiphaseflow.2020.103219, 2020.

Bradski, G.: The OpenCV Library, Dr. Dobb's J. Softw. Tools, 25, 120–125, 2000.

Buades, A., Coll, B., and Morel, J.-M.: Non-Local Means Denoising, Image Process. On Line, 1, 208–212, https://doi.org/10.5201/ipol.2011.bcm_nlm, 2011.

Castanet, G., Dunand, P., Caballina, O., and Lemoine, F.: High-speed shadow imagery to characterize the size and velocity of the secondary droplets produced by drop impacts onto a heated surface, Exp. Fluids, 54, 1489, https://doi.org/10.1007/s00348-013-1489-3, 2013.

Chong, Z. Z., Tor, S. B., Gañán-Calvo, A. M., Chong, Z. J., Loh, N. H., Nguyen, N.-T., and Tan, S. H.: Automated droplet measurement (ADM): an enhanced video processing software for rapid droplet measurements, Microfluid. Nanofluid., 20, 66, https://doi.org/10.1007/s10404-016-1722-5, 2016.

De Cock, N., Massinon, M., Nuyttens, D., Dekeyser, D., and Lebeau, F.: Measurements of reference ISO nozzles by high-speed imaging, Crop Prot., 89, 105–115, https://doi.org/10.1016/j.cropro.2016.07.016, 2016.

Fenn, J. B., Mann, M., Meng, C. K., Wong, S. F., and Whitehouse, C. M.: Electrospray ionization for mass spectrometry of large biomolecules, Science, 246, 64–71, https://doi.org/10.1126/science.2675315, 1989.

https://doi.org/10.5194/ar-2026-52
Preprint. Discussion started: 24 November 2026
© Author(s) 2026. CC BY 4.0 License.



Gañán-Calvo, A. M.: Enhanced liquid atomization: From flow-focusing to flow-blurring, Appl. Phys. Lett., 86, 214101, https://doi.org/10.1063/1.1931057, 2005.

Gañán-Calvo, A. M., López-Herrera, J. M., Herrada, M. A., Ramos, A., and Montanero, J. M.: Review on the physics of electrospray: from electrokinetics to the operating conditions of single and coaxial Taylor cone-jets, and AC electrospray, J. Aerosol Sci., 125, 32–56, https://doi.org/10.1016/j.jaerosci.2018.05.002, 2018.

Hermosín-Reyes, M., Gañán-Calvo, A. M., and Modesto-López, L. B.: Flow blurring atomization of poly(ethylene oxide) solutions below the coil overlap concentration, J. Aerosol Sci., 137, 105429, https://doi.org/10.1016/j.jaerosci.2019.105429, 2019.

Hu, M.-K.: Visual pattern recognition by moment invariants, IRE Trans. Inf. Theory, 8, 179–187, https://doi.org/10.1109/TIT.1962.1057692, 1962.

Jaworek, A.: Micro- and nanoparticle production by electrospraying, Powder Technol., 176, 18–35, https://doi.org/10.1016/j.powtec.2007.01.035, 2007.

Jaworek, A. and Sobczyk, A. T.: Electrospraying route to nanotechnology: an overview, J. Electrostat., 66, 197–219, https://doi.org/10.1016/j.elstat.2007.10.001, 2008.

Law, S. E.: Agricultural electrostatic spray application: a review of significant research and development during the 20th century, J. Electrostat., 51–52, 25–42, https://doi.org/10.1016/S0304-3886(01)00040-7, 2001.

Lefebvre, A. H. and McDonell, V. G.: Atomization and Sprays, 2nd edn., CRC Press, Boca Raton, USA, https://doi.org/10.1201/9781315120911, 2017.

Li, D., Bothell, J. K., Morgan, T. B., Machicoane, N., Aliseda, A., Kastengren, A. L., and Heindel, T. J.: Time-averaged spray analysis in the near-field region using broadband and narrowband X-ray measurements, Atomization Spray, 29, 331–349, https://doi.org/10.1615/AtomizSpr.2019030744, 2019.

Lucas, B. D. and Kanade, T.: An iterative image registration technique with an application to stereo vision, in: Proceedings of the 7th International Joint Conference on Artificial Intelligence (IJCAI 1981), Vancouver, Canada, 24–28 August 1981, 674–679, 1981.

Marín-Brenes, F., Olmedo-Pradas, J., Gañán-Calvo, A. M., and Modesto-López, L. B.: On the ejection of filaments of polymer solutions triggered by a micrometer-scale mixing mechanism, Materials, 14, 3399, https://doi.org/10.3390/ma14123399, 2021.

Modesto-López, L. B. and Gañán-Calvo, A. M.: Visualization and size-measurement of droplets generated by Flow Blurring® in a high-pressure environment, Aerosol Sci. Technol., 52, 198–208, https://doi.org/10.1080/02786826.2017.1390207, 2018.

Modesto-López, L. B., Pérez-Arjona, A., and Gañán-Calvo, A. M.: Flow Blurring-enabled production of polymer filaments from poly(ethylene oxide) solutions, ACS Omega, 4, 2693–2701, https://doi.org/10.1021/acsomega.8b02542, 2019.

https://doi.org/10.5194/ar-2026-52
Preprint. Discussion started: 24 November 2026
© Author(s) 2026. CC BY 4.0 License.



1030 Nuyttens, D.: Drift from field crop sprayers: The influence of spray application technology determined using indirect and direct drift assessment means, PhD thesis, Katholieke Universiteit Leuven, Belgium, 293 pp., available at: http://hdl.handle.net/1979/1047, 2007.

Pérez-Cantalapiedra, C., Carranza-García, M., and Modesto-López, L. B.: Statistical analysis of droplet trajectories in
1035 electrically assisted Flow Blurring sprays, Zenodo [data set], https://doi.org/10.5281/zenodo.24201211, 2026.

Privitera, S., Manetto, G., Pascuzzi, S., Pessina, D., and Cerruto, E.: Drop size measurement techniques for agricultural sprays: A state-of-the-art review, Agronomy, 13, 678, https://doi.org/10.3390/agronomy13030678, 2023.

1040 Ramos-Escobar, A., Uceda-Gallegos, R., Modesto-López, L. B., and Gañán-Calvo, A. M.: Dynamics of formation of poly(vinyl alcohol) filaments with an energetically efficient micro-mixing mechanism, Phys. Fluids, 32, 122101, https://doi.org/10.1063/5.0030494, 2020.

Rosell-Llompart, J. and Gañán-Calvo, A. M.: Turbulence in pneumatic flow focusing and flow blurring regimes, Phys. Rev.
1045 E, 77, 036321, https://doi.org/10.1103/PhysRevE.77.036321, 2008.

Russ, J. C.: The Image Processing Handbook, 6th edn., CRC Press, Boca Raton, USA, https://doi.org/10.1201/b10720, 2011.

Shrimpton, J. S.: Charge Injection Systems: Physical Principles, Experimental and Theoretical Work, Heat and Mass Transfer,
1050 Springer, Berlin, Heidelberg, https://doi.org/10.1007/978-3-642-00294-6, 2009.

Shrimpton, J. S. and Yule, A. J.: Electrohydrodynamics of charge injection atomization: regimes and fundamental limits, Atomization Spray, 13, 173–190, https://doi.org/10.1615/AtomizSpr.v13.i23.20, 2003.

1055 Sijs, R., Kooij, S., Holterman, H. J., van de Zande, J., and Bonn, D.: Drop size measurement techniques for sprays: Comparison of image analysis, phase Doppler particle analysis, and laser diffraction, AIP Adv., 11, 015315, https://doi.org/10.1063/5.0018667, 2021.

Simmons, B. M. and Agrawal, A. K.: Flow blurring atomization for low-emission combustion of liquid biofuels, Combust.
1060 Sci. Technol., 184, 660–675, https://doi.org/10.1080/00102202.2012.660222, 2012.

Sirignano, W. A.: Fluid Dynamics and Transport of Droplets and Sprays, 2nd edn., Cambridge University Press, Cambridge, UK, https://doi.org/10.1017/CBO9780511806728, 2010.

1065 Suzuki, S. and Abe, K.: Topological structural analysis of digitized binary images by border following, Comput. Vis. Graph. Image Process., 30, 32–46, https://doi.org/10.1016/0734-189X(85)90016-7, 1985.

Wang, Z., Wen, J. Z., Wang, J., and Dong, Q.: PDPA investigation on an electrostatically-assisted twin-fluid atomization flow. Adv. Mech. Eng., 6, Article 402747, 10 pp. https://doi.org/10.1155/2014/402747, 2014.

1070

Zuiderveld, K.: Contrast Limited Adaptive Histogram Equalization, in: Graphics Gems IV, edited by: Heckbert, P. S., Academic Press, San Diego, USA, 474–485, https://doi.org/10.1016/B978-0-12-336156-1.50061-6, 1994.